Applied Catalysis B: Environmental 282 (2021) 119612

Contents lists available at ScienceDirect

Applied Catalysis B: Environmental

journal homepage: www.elsevier.com/locate/apcatb

New insights into the efficient charge transfer of ternary chalcogenides composites of TiO_2

Priyanka Ganguly[a,b], Syam Kumar R.[c], Marica Muscetta[d], Nisha T. Padmanabhan[e,f], Laura Clarizia[d], A. Akande[c], Steven Hinder[g], Snehamol Mathew[a,b], Honey John[e,f], Ailish Breen[a,b], Suresh C. Pillai[a,b,*]

[a] Nanotechnology and Bio-engineering Research Group, Department of Environmental Science, Institute of Technology Sligo, Sligo, Ireland
[b] Centre for Precision Engineering, Materials and Manufacturing Research (PEM), Institute of Technology Sligo, Sligo, Ireland
[c] Mathematical Modelling Research Group, Department of Health and Nutritional Science, Institute of Technology Sligo, Sligo, Ireland
[d] Dipartimento di Ingegneria Chimica, dei Materiali e della Produzione Industriale, Università di Napoli Federico II, p. le V. Tecchio 80, 80125 Napoli, Italy
[e] Department of Polymer Science and Rubber Technology, Cochin University of Science and Technology, Kerala 682022, India
[f] Inter University Centre for Nanomaterials and Devices (IUCND), Cochin University of Science and Technology, Kerala 682022, India
[g] The Surface Analysis Laboratory, Faculty of Engineering and Physical Sciences, University of Surrey, Guildford, Surrey, GU2 7XH, United Kingdom

ARTICLE INFO

Keywords:
Photocatalysis
Band edge alignment
Water splitting
Antimicrobial inactivation
Antibiotics degradation
Computational study

ABSTRACT

A two-step solvothermal synthesis was adopted to prepare $AgXSe_2$-TiO_2 (X = In, Bi) composites. DFT study of the pristine parent samples showed the formation of the hexagonal phase of $AgBiSe_2$, and tetragonal phase of $AgInSe_2$ and TiO_2, which corroborated the experimentally synthesised structures. Both the $AgBiSe_2$-TiO_2 and $AgInSe_2$-TiO_2 composites displayed enhanced visible light absorption and reduced band gap in the UV-DRS patterns. The XPS results exhibited a shift in binding energy values and the TEM results showed the formation of spherical nanoparticles of both $AgBiSe_2$ and $AgInSe_2$. The PL signals displayed delayed recombination of the photogenerated excitons. The as synthesised materials were studied for their photocatalytic efficiency, by hydrogen generation, degradation of doxycycline, and antimicrobial disinfection (*E. coli* and *S. aureus*). The composite samples illustrated more than 95 % degradation results within 180 min and showed 5 log reductions of bacterial strains within 30 min of light irradiation. The hydrogen production outcomes were significantly improved as the $AgBiSe_2$ and $AgInSe_2$ based composites illustrated 180-fold and 250-fold enhanced output compared to their parent samples. The enhanced photocatalytic efficiency displayed is attributed to the delayed charge recombination of the photogenerated electron-hole pairs in the $AgXSe_2$-TiO_2 interface. Formation of a *p-n* nano heterojunction for $AgBiSe_2$-TiO_2 and type II heterojunction for $AgInSe_2$-TiO_2 composite are explained.

1. Introduction

The ever-increasing need for energy for a growing population amidst depleting natural resources has resulted in the search for cleaner, greener and cheaper energy alternatives. Photocatalysis is one of the central alternatives in this regard. The distinct advantage of this process is that is does not requiring any complicated systems or accessories. [1–3] It only requires a potential photocatalyst which is dispersed in water and irradiated under visible light or sunlight. However, for any good process there exist certain disadvantages [4]. The search for an optimum catalyst that could be commercialised in large scale for various photocatalytic applications is yet to be achieved [5]. Quicker recombination, poor light-harvesting ability and recovery of the catalyst after use are some of the major challenges. Hence, there is a research drive to seek out for new generation materials to enhance the reported efficiency [6]. Semiconductor photocatalysis has emerged as an exciting solution lately, as reports of new hybrids and nanoarchitectures has resulted in several functional applications, such as sensors, CO_2 reduction, hydrogen generation, degradation and antimicrobial disinfection *etc* [7]. These nanomaterials show characteristic absorptions, in the ultra-violet region, visible and some instances of the near-infrared region [8,9]. Semiconductor materials such as TiO_2 and ZnO are stable, non-toxic and easy to synthesise. However, these materials have a wide band gap which result in absorption of light at the

* Corresponding author at: Nanotechnology and Bio-engineering Research Group, Department of Environmental Science, Institute of Technology Sligo, Sligo, Ireland.
E-mail address: pillai.suresh@itsligo.ie (S.C. Pillai).

https://doi.org/10.1016/j.apcatb.2020.119612
Received 30 July 2020; Received in revised form 30 September 2020; Accepted 5 October 2020
Available online 08 October 2020

UV region of the electromagnetic spectrum. The absorption of UV light which accounts for only a small portion is a severe concern to these traditional semiconductor nanomaterials. In contrast, metal chalcogenides have shown exciting applications across photochemistry. However, the search for new, less toxic, narrow band gap semiconductor materials has resulted in the formation of ternary and even quaternary combination of elements to form multi-class chalcogenide compounds. [10–12]

Ternary chalcogenides (TC) are a fascinating class of semiconductor nanomaterials with narrow band gaps suitable for light-harvesting ability in the entire domain of visible and small region of infrared band of the electromagnetic spectrum. [8,13,14] In a ternary combination of ABX, where X denotes the chalcogens (S, Se and Te), B is the lattice forming elements with their oxidation states denoted beside and A is a variable metal, that could be of +1 (Cu/Ag) or +2 (Zn/Cd) oxidation states resulting in the formation of ABX_2 or AB_2X_4 compounds respectively. [15,16] The presence of multiple probabilities for chemical substitutions amongst the three-element combination (ternary chalcogenides) and the structural modifications (formation of rods, needles, tubes and flowers *etc.*) provides substantial opportunity to tune the essential properties for desired applications. [17,18] Along with the versatility of stoichiometric compositions, TCs also exhibits a vast range of stable and metastable nanocrystalline compounds. The stoichiometric composition and the size of the nanoparticles of the TC influences in broad variability of the light absorption. The optical properties are modified by the quantum size effects, which results in enhanced absorption. Numerous approaches such as solid-state sintering, solid solution technique, flux technique, microwave-assisted method, hydro/solvothermal procedure, polyol route and sonochemical techniques are used to synthesise TCs. [18–21] The use of deposition techniques has been widely observed to be successful and effective in controlling the stoichiometric ratios of the elemental combination [22]. However, colloidal chemistry has proven equally efficient in controlling the stoichiometric ratios of the atomic combination in these TC compounds. Interesting morphologies and nanoarchitectures have been observed as a result of tweaking multiple factors. Selection of the organic solvent, the temperature and the use of any surfactant/ligand is vital in developing the synthesis [23,24]. Nevertheless, the absence of a standard protocol for such synthesis is one of the significant hurdles to replicate the process in synthesising various other binary and ternary chalcogenide compounds. Reports of the use of these multicomponent elemental compounds as potential materials for heterojunction formation with traditional semiconductor nanomaterials such as metal oxides and other two-dimensional nanomaterials is relatively new. The narrow band gap of these compounds with a combination of wide band gap semiconductors has resulted in efficient heterostructures for multifunctional applications. Silver-based ternary compounds are not new to the research realm [20,25–27]. Ag-X-Se compounds with X (lattice forming elements) atoms with +3 (In) and +5 (Bi) oxidation states, are reported for various multifunctional applications such as for solar cell applications, high thermoelectric performance, dye degradation, as quantum dots for bioimaging *etc.* [18,19,28]

$AgBiSe_2$ exists in three crystalline phases. The commonly synthesised crystal structure is the hexagonal phase (space group $Pm\bar{3}1$), transitions to a rhombohedral phase (space group $R\bar{3}m$). [29] The rhombohedral phase is the intermediate phase (transition at 137 °C) which finally leads into a cubic phase at 297 °C (space group $Fm\bar{3}m$) [30]. In the rhombohedral phase, the silver and the bismuth cations occupy ordered positions, while in the cubic phase, these atoms get disordered. The hexagonal and rhombohedral nanomaterials are narrow band gap semiconductors, whereas the cubic phase behaves as metal. Similarly, $AgInSe_2$ exists mostly in two different crystalline phases. The thermodynamically stable tetragonal phase (space group I42D), which transitions into a metastable orthorhombic phase at a higher temperature (space group $Pna2_1$). [15,31]

Studies on heterostructure formation with $AgBiSe_2$ nanoparticles are yet to be reported. Whereas, $AgInSe_2$ based composites have displayed numerous applications. [32,33] Chen *et al.* reported the deposition of $AgInSe_2$ nanoparticles onto TiO_2 films for solar cell application. The films of the composite displayed a significant increase in efficiency. [34] In a different study, Li et al. reported the synthesis of functionalised quantum dots with different types of organic molecules. The functionalised quantum dots displayed potential applications as light harvesters in quantum dot sensitised solar cell (QSSC) [35]. In a recent report, Kshirsagar et al. reported the composite of $AgInSe_2$ nanoparticles with TiO_2 for photocatalytic dye degradation. The $AgInSe_2$ nanoparticles were synthesised using microwave and thermal irradiation. The composite displayed enhanced degradation result compared to their parent samples.[36] Thus, it shows the enormous potential of these composites and ushers the importance of their untapped potential for various other applications.

Compared to other synthesis procedures, the reported synthesis method is found to be inexpensive and evades any kind of complicated deposition or precursor injection methods. This study provides a direction for optimising the process conditions such as the time and temperature of the solvothermal synthesis. Composites of titania with these two different TC are formed at different weight ratios (0.5, 1, 2, 5 wt %). The as prepared composites are analysed using structural, elemental and morphological characterisation techniques. Furthermore, the efficiency of these composites is studied using three different photocatalytic applications; hydrogen generation, Doxycycline (DC) degradation and antimicrobial disinfection. The results of all the characterisations and the applications are compared to their parent nanostructures.

2. Synthesis and method

2.1. Computational details

All the computational calculations were performed using the Vienna Ab initio Simulations Package (VASP) based on Density Functional Theory (DFT). [37] Standard generalized gradient approximation (GGA) within the Perdew-Burke-Ernzerhof (PBE) was used as the exchange-correlation functional to relax the geometries of TiO_2, $AgInSe_2$ and $AgBiSe_2$ [38]. It is known that PBE reproduces these structures well, but at the same time, it is affected by the self-interaction correction leading to the systematic underestimation of the band gap of these materials [39]. The projector-augmented wave (PAW) method with the plane-wave basis-set cut-off of 520 eV and a Monkhorst-Pack (MP) grid of 8 × 8 × 5 k-points were used [40–42]. The convergence criterion is that the forces on individual atoms are less than 0.001 eV/ Å and the total energy of 1×10^{-7} eV per atom. The ground-state electronic structure calculations have been carried out using 4 × 4 × 3 MP k-grid and the hybrid Heyd-Scuseria-Ernzerhof (HSE06) exchange-correlation functional. [43,44] HSE06 is a nonlocal, range separated, screened Coulomb potential density functional that provides accurately the electronic properties that match the experimental results [45].

The position of conduction band minima (CBM) and valence band maxima (VBM) were determined by the calculated HSE06 band gap (E_g) using the following equations;[46]

$$E_{CBM} = (\chi_A^x \chi_B^y \chi_C^z)^{\frac{1}{x+y+z}} - \frac{1}{2}E_g + E_0 \quad (1)$$

$$E_{VBM} = E_{CBM} + E_g \quad (2)$$

in which χ_A, χ_B and χ_C stand for the absolute electronegativities of A, B and C atoms respectively where the compound under consideration has the chemical formula $A_xB_yC_z$. E_0 is 4.5 eV for the normal hydrogen electrode (NHE) and it relates the reference electrode redox level to absolute vacuum scale. From the Pearson electronegativity table, the values of χ_{Ti}, χ_O, χ_{Ag}, χ_{In}, χ_{Bi} and χ_{Se} were obtained as 3.45, 7.54, 4.44, 3.10, 4.69 and 5.89 eV respectively.

2.2. Synthesis of $AgXSe_2$-TiO_2 (X = In, Bi) composite

Synthesis of $AgXSe_2$ – TiO_2 (X = In, Bi) composite was prepared using sol-gel method and solvothermal synthesis subsequently. Firstly, the TiO_2 was synthesised using the sol-gel method, taking titanium isopropoxide (TTIP) as the precursor. The water was added dropwise to the TTIP taken in isopropanol under vigorous stirring. For the gel formation, the water and TTIP ratio was considered 1:1 in an isopropanol solution mixture. The resultant solution was kept for gelation for 2 h. Then it was dried in an oven for 12 h at 100 °C to remove the excess solvent. The resultant xerogel was calcined at 500 °C, at a ramp rate of 10 °C/min for 2 h to get anatase TiO_2.

Secondly, the $AgXSe_2$-TiO_2 heterostructure composites were prepared by using the solvothermal method. Where X is the lattice forming elements (In or Bi). 30 mL of ethanolamine was taken in a beaker and a definite amount of $AgNO_3$, $In(NO_3)_3.xH_2O$ and $SeCl_4$ at a ratio of 1:1:2 was added under vigorous stirring. The solution was kept stirring for 1 h at RT, and formerly prepared TiO_2 was added to this mixture. This mixture was ultra-sonicated for another 30 min. The amount of TiO_2 was added, in such that the final composites result in the desired ratio of 0.5, 1, 2 & 5 wt % $AgInSe_2$ with TiO_2. The resultant mixture solution was placed in a 50 mL steel Teflon vessel (from Parr instruments) and heated for 24 h at 180 °C. The solid product formed was washed with water and ethanol multiple times to remove the solvent residue and kept for drying overnight at 60 °C. The resultant product was used for further characterisation and applications. The similar procedure was repeated for synthesising $AgBiSe_2$ – TiO_2, by taking $Bi(NO_3)_3.5H_2O$ as the precursor. The parent samples ($AgInSe_2$ and $AgBiSe_2$) were synthesised without adding TiO_2. The materials, characterisation details and all the photocatalytic experimental process is provided in supporting information.

3. Results and discussions

3.1. Structural properties

After the structural optimization using DFT studies, the space groups of anatase TiO_2, $AgInSe_2$ and $AgBiSe_2$ were found to be $I4_1/amd$ (space group number: 141), $I\bar{4}2d$ (space group number: 122) and $P\bar{3}m1$ (space group number: 164), respectively. TiO_2 and $AgInSe_2$ were found to crystallize into a body-centred tetragonal crystal system upon relaxation while $AgBiSe_2$ was found to be stable in a hexagonal lattice. The lattice parameters and volume of the three compounds obtained after structural optimization are tabulated in Table S1, and the optimized structures are presented in Figure S2 and Fig. 1. The lattice parameters of these compounds obtained after structural optimization are consistent with the reported ones. They are arranged well within the expected error range when compared to the experimental values observed in section 3.3 [39,47,48]. Octahedral molecular geometry connects Ti and O in the case of anatase TiO_2. These octahedra are connected to each other by edge sharing at the centre of the unit cell and corner sharing elsewhere in the unit cell. There are two different Ti-O bond lengths present in the compound. The in-plane Ti-O bond length was found to be 1.94 Å and the out-of-plane Ti-O bond length was 2.00 Å which are well consistent with the ones that could be obtained from the literature. [39,49]

In the case of $AgInSe_2$, In and Se are connected to each other in a tetrahedral molecular geometry. These tetrahedra are connected to each other through corner sharing, and Ag is found to occupy the interstitial sites of these tetrahedra. In-Se bond lengths are isotropic in this compound and yields a value of 2.65 Å. $AgBiSe_2$ is a layered material where Ag intercalates the Bi-Se octahedra. The Bi-Se bond length is found to be 2.99 Å and is isotropic within the octahedral molecular geometry. The octahedra are connected to each other through edge sharing.

3.2. Electronic properties

Since the HSE calculations has been known to reproduce the electronic properties of materials accurately, it has been adopted to investigate the electronic properties of these compounds. Starting with anatase TiO_2, its band structure and corresponding partial density of states (PDOS) are presented in Figure S3. Ti *d*-orbitals dominate the lower CB while the O *p*-orbitals are found to dominate the upper VB of TiO_2. The HSE06 calculation returns the band gap of 3.35 eV for TiO_2, which is consistent with the experimentally observed value (Section 3.4) and in the reported literature. [39,49] Anatase TiO_2 is an indirect band gap material with its CBM positioned at the centre of the Brillouin zone, Γ and the VBM between P and Y.

$AgBiSe_2$ presents a band gap of 0.55 eV. Other works have reported values ranging from 0.6 eV to 0.8 eV. [47,50] It should, however, be noted that the experimentally observed value is 1.22 eV, which is ~0.4 eV more than the reported values in the literature. It is worth mentioning that the HSE functional has been reported to underestimate experimental bandgaps in some systems [51]. The difference in band gap can be attributed to different cell volumes of the computed and experimental unit cells, and the possible site-occupation disorders present in the experimental sample [52]. The HSE06 band structure and PDOS are presented in Fig. 2. $AgBiSe_2$ is an indirect band gap material with its CBM placed at the high symmetry point, A and the VBM between K and Γ of the Brillouin zone. The upper VB is dominated by the Ag 4*d* and Se 4*p* states. The lower CB of $AgBiSe_2$ is dominated by the combination of Bi 6p and Se 4p states.

$AgInSe_2$, in its tetragonal lattice, is found to have an HSE06 band gap of 1.2 eV, which matches the reported values in the literature. [48,53] The electronic structure and the PDOS of $AgInSe_2$ are shown in Fig. 3. $AgInSe_2$ is a direct band gap material at Γ. Interestingly, Ag 4*d* states and Se 4*p* states dominate the upper VB while In 5*s* and Se 4*p* states contribute to the lower CB of $AgInSe_2$.

The band edge values of TiO_2, $AgInSe_2$ and $AgBiSe_2$ are presented in Table S2. The reference scale was NHE which keeps the hydrogen evolution reaction (HER) potential at 0 eV and the oxygen evolution reaction (OER) potential at 1.23 eV. Looking into the band edge positions of the pristine compounds, it could be observed that $AgInSe_2$ could aid the HER and $AgBiSe_2$ on its own fails to aid either of the reaction paths.

3.3. Synthesis and structural analysis by X-ray diffraction

The synthesis process of the $AgXSe_2$-TiO_2 is displayed in Fig. 4. As explained in section 2.2, $AgXSe_2$ nanoparticles were synthesised using a solution-based technique. Organic solvents such as oleylamine, diethanolamine has been used previously to produce various types of TCs. In this study, ethanolamine was used as the solvent for the solvothermal synthesis. Ethanolamine (EA) has a high boiling point and act as a stabilising agent in the synthesis process, hence making it a perfect choice of solvent. Unlike the sintering technique, with long annealing times and need for high temperatures, in the solvothermal process, this is easily evaded. Amine based solvents usually lower the temperature for thermal decomposition of the precursors and aid in the formation of nanoparticles at a lower temperature. [54] They are often used as a potential reagent for anisotropic growth of nanoparticles as well as surfactants for a possible stabilising agent [15]. At the start, the Ag^+, In^{3+} and Bi^{3+} ions react with the solvent molecules (ethanolamine) to form a covalent complex as given below (where x and y are positive integers). [55,56]

$$AgNO_3 + EA \rightarrow Ag(EA)_x^+ + NO_3^- \quad (3)$$

$$Bi(NO_3)_3 + EA \rightarrow Bi(EA)_y^{3+} + 3NO_3^- \quad (4)$$

$$In(NO_3)_3 + EA \rightarrow In(EA)_y^{3+} + 3NO_3^- \quad (5)$$

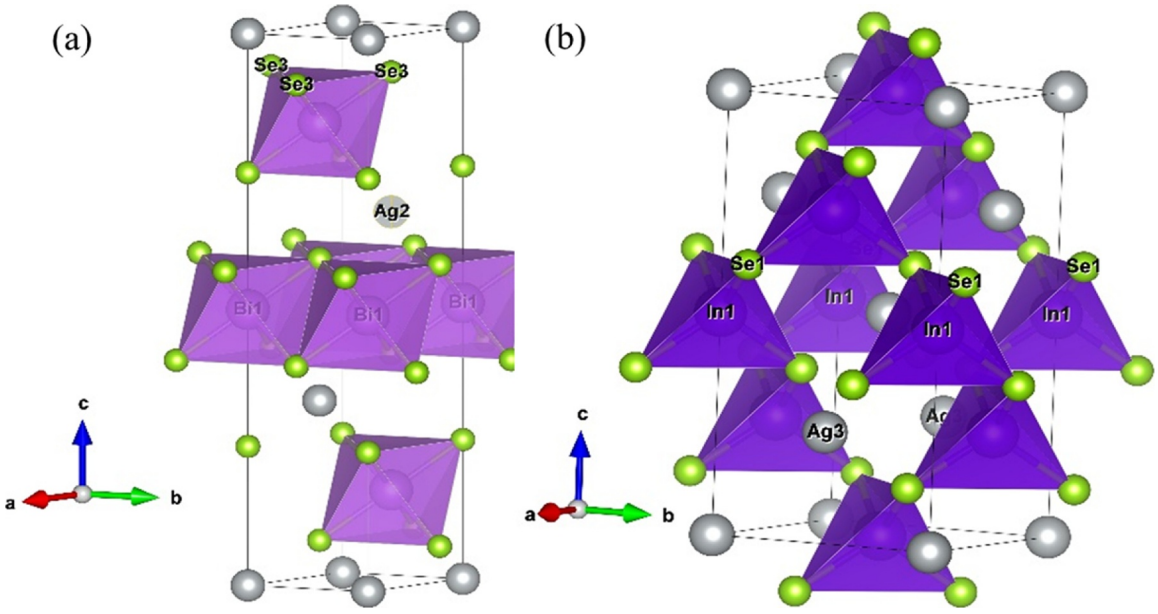

Fig. 1. The optimised structures of (a) $AgBiSe_2$, (b) $AgInSe_2$.

Furthermore, the silver complexes react with the Se^{2-} ions to form binary compound; [57]

$$Ag(EA)_x^+ + Se^{2-} \rightarrow Ag_2Se + EA \quad (6)$$

As explained by Bai et al., the initial species formed in the process

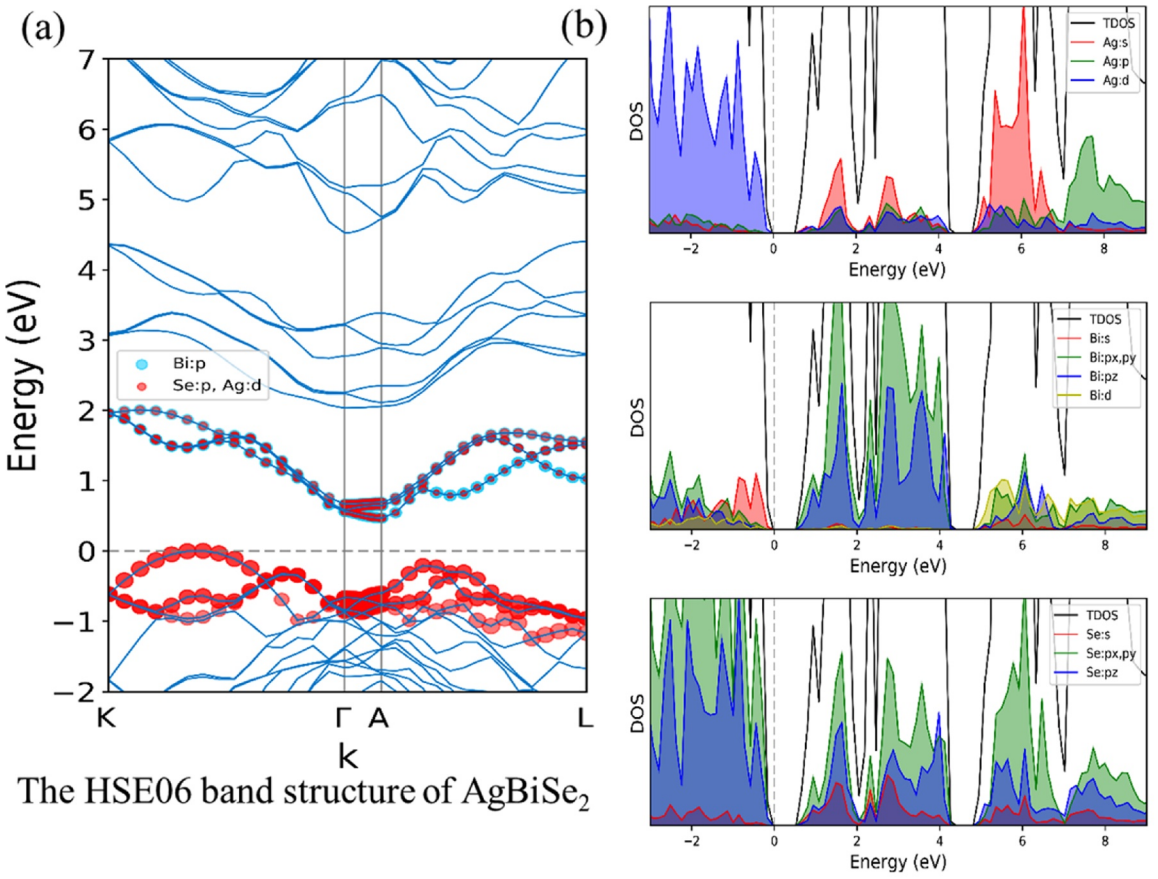

The HSE06 band structure of $AgBiSe_2$

Starting from top, the PDOS of $AgBiSe_2$ presenting the states of Ag, Bi and Se.

Fig. 2. The HSE06 (a) band structure and (b) PDOS of $AgBiSe_2$. The PDOS plot is split into two to describe the Ag, Bi and Se states separately. Ag 4*d* and Se 4*p* states dominate the upper VB while the Se 4*p* and Bi 6*p* states are dominating the lower CB.

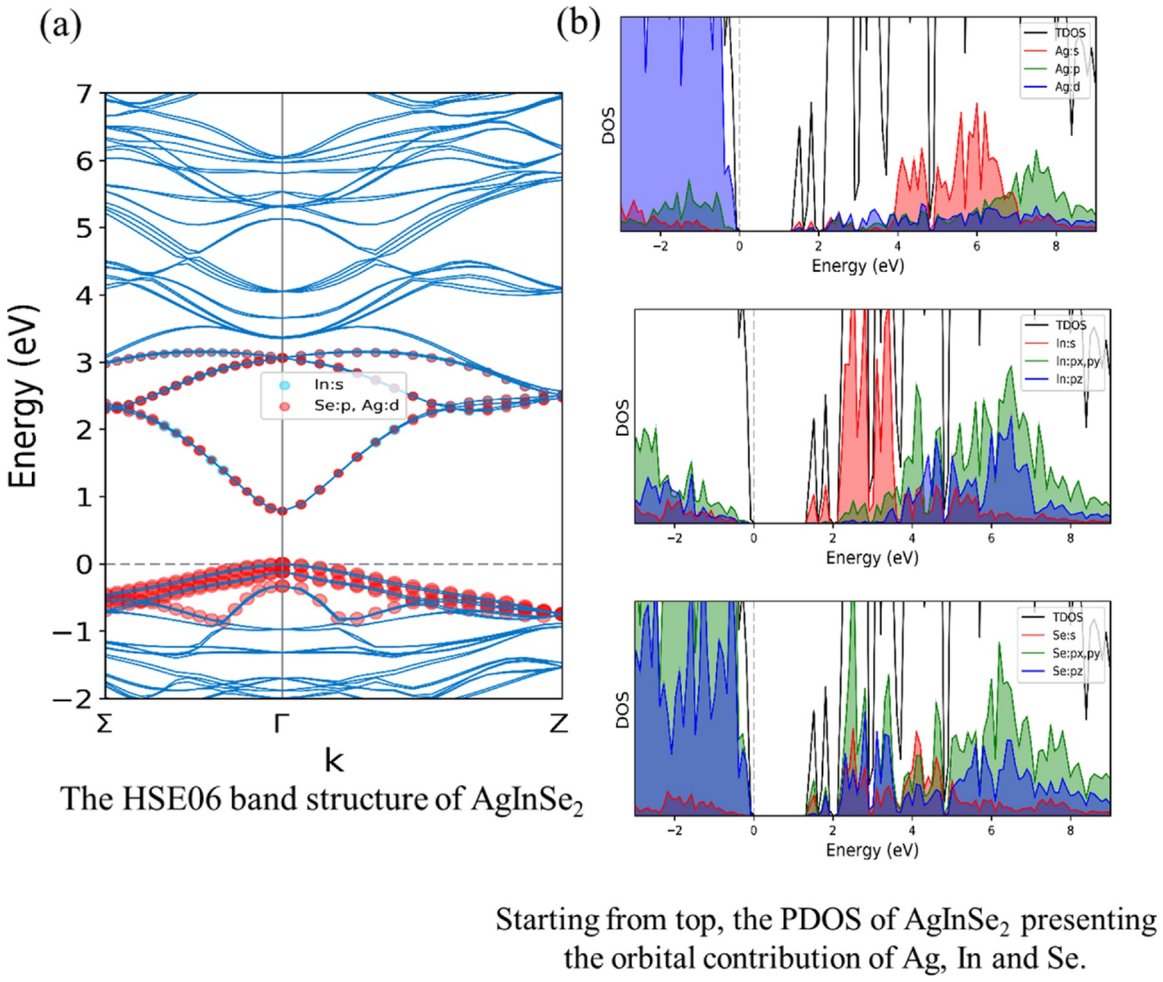

Fig. 3. The HSE06 (a) band structure and (b) PDOS of anatase $AgInSe_2$. The PDOS plot is split into two to describe the Ag, In and Se states separately. Ag 4*d* and Se 4*p* states dominate the upper VB while the Se 4*p* and In 5*s* states are dominating the lower CB.

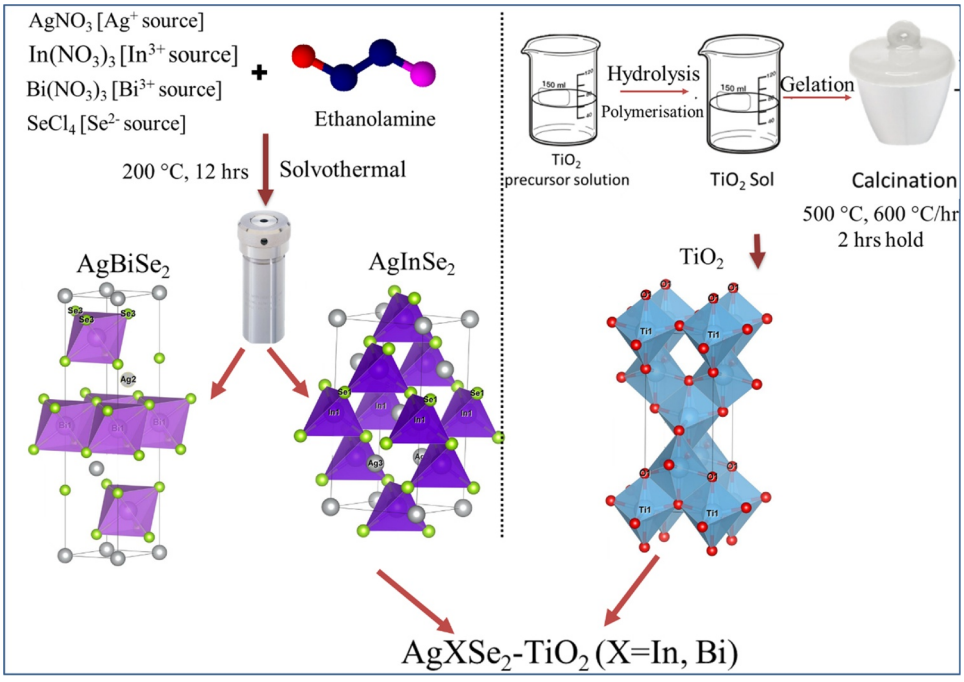

Fig. 4. Schematic illustration of the synthesis process of $AgXSe_2$-TiO_2.

are the orthorhombic phase of Ag_2Se spherical nanoparticles [58]. The fluid-like nature of the silver and fast conducting behaviour of silver chalcogenides result in the creation of various cationic vacancies in the orthorhombic crystal structure. This results in fast diffusion of Bi^{3+} and In^{3+} ions to form heterostructures of $AgBiSe_2$-Ag_2Se and $AgInSe_2$-Ag_2Se, respectively. As the synthesis progresses, the diffusion phenomenon continues, until all the Ag_2Se seeds are exhausted. This could also be observed in the temperature and the time study graphs of the TC (Figure S4 and S5). The peaks of Ag_2Se are present at lower reaction time and temperature, and as the reaction progresses the intensity of the peak starts to diminish, leaving a residue of a small percent of impurity. The XRD of the as synthesised $AgBiSe_2$ and $AgInSe_2$ is compared with the JCPDS patterns of the hexagonal structure of $AgBiSe_2$ [ICDD card no: 04-010-1589] and the tetragonal structure of $AgInSe_2$ [ICDD card no: 00-035-1099] in Figure S6 of the supporting information [15,58,59].

$$Ag_2Se + Bi(EA)_y^{3+} \rightarrow AgBiSe_2 + EA \quad (7)$$

$$Ag_2Se + In(EA)_y^{3+} \rightarrow AgInSe_2 + EA \quad (8)$$

Ethanolamine (EA), with a single amine and N-chelating atom, act as a potential structure directing agent [60]. The inbuilt pressure and the appropriate temperature supports the formation of unique phases and morphology. This results in the formation of spherical nanoparticles of $AgInSe_2$ in tetragonal phase and $AgBiSe_2$ in hexagonal phase, respectively.

The nanoparticles ($AgXSe_2$) and the composites with titania were examined using X-ray diffraction. Formation of hexagonal phase $AgBiSe_2$ and tetragonal phase of $AgInSe_2$ nanoparticles are observed in Fig. 5a and b [ICDD card no: 04-010-1589 and 00-035-1099]. The influence of the solvothermal duration and the temperature to identify the optimised experimental parameters were also studied (Figure S4 and S5). As observed, the intensity (100 %) of the peaks at 30.62° for $AgBiSe_2$ and 25.68° for $AgInSe_2$ are found to be sharp and well defined. This infers the formation of crystalline structures at 200 °C and 12 h of solvothermal duration. Hence, 200 °C and 12 h is the optimal temperature and time for the synthesis process and henceforth used for composite preparation with titania nanoparticles. The sol-gel synthesis of TiO_2 and its further calcination at 500 °C leads to the formation of the anatase phase. Defined peaks at 25.1° corresponding to the tetragonal structure of the anatase phase are observed [ICDD card no: 00-021-1272]. The lattice parameter of the parent samples were estimated to be; hexagonal phase of $AgBiSe_2$ with a = b = 4.17 Å, c = 19.72 Å and $\alpha = \beta = 90^\circ$ and $\gamma = 120^\circ$. While the tetragonal crystal structure of $AgInSe_2$ displayed a = b = 6.41 Å, c = 12.25 Å and $\alpha = \beta = \gamma = 90^\circ$. Pristine titania [tetragonal phase] have lattice parameter estimated to be a = b = 3.71 Å, c = 9.43 Å and $\alpha = \beta = \gamma = 90^\circ$. These values are similar to the values obtained through the computational study, as explained in section 3.1.

Fig. 8a and b further display the composites prepared at various weight ratios (0.5, 1, 2 and 5 wt%). This study particularly aims in understansing the effect of TC at lower weight ratios*(< 5 wt%)* to a wide band gap semiconductor such as titania. Understanding of TC nanomaterials at higher weight ratios and its optimisation will be carried out in future studies. The higher content will lead to various composite combinations and would be difficult to compare with the existing line of discussions. Peaks at 25.1° of titania in the anatase phase are observed for all the composite structures irrespective of the weight ratios. The broadening of the peaks demonstrates that the crystalline size of the sample is minimal. Peaks of TCs are not observed prominently in any of the diffractograms, except for the 5 wt% $AgBiSe_2$-TiO_2, where a small peak at 30.6° is detected. The incorporation of TCs in very small weight ratios and the crystalline nature of the titania nanoparticles makes it difficult to observe any distinct peaks of TCs in the diffractograms. Furthermore, it also validates that the structure of TiO_2 remains unaltered even after the solvothermal reaction for the composite formation.

3.4. Absorption properties

UV–vis DRS measurements were taken of the as prepared samples to study their light absorption characteristics. As shown in Fig. 6a and b, the pristine TiO_2 displays its signature absorption at 320 nm in the UV region, and the absorption edge steeps at 400 nm. Fig. 6a also displays the absorption spectra of the $AgBiSe_2$-TiO_2 composites. The absorption pattern displays a combination of both the parent samples. All the samples show the signature hump of titania at 320 nm, with absorption extending throughout the visible region, typical to the pattern as observed for $AgBiSe_2$ (Figure S7a). [19] Increase in the content of TC in the sample resulted in increased absorption in the visible region. Similarly, Fig. 6b shows the absorption spectra of the $AgInSe_2$-TiO_2 composites. Like the previous composite samples, they also displayed a common pattern. All the samples carried the signature profile of titania. In contrast, an increase in the content of the TC in the prepared sample, resulted in an increase in absorption in the visible region as defined by its parent $AgInSe_2$ (Figure S7b). [58] This was further reflected in the change in the colour of the samples, varying from white to brown and further black. This demonstrated the coupling of TCs with titania to construct $AgXSe_2$-TiO_2 composites.

Band gap engineering of the semiconductors is the prime aspect of the heterojunction construction. Thus, the influence of the TC addition to TiO_2 could be further observed by the changes in the band gap of the composite sample. The Kubelka-Munk (K-M) function is utilised to convert the functionality to energy (Figure S8a and S8b). [61] The extrapolation of the lines in the plots enables to evaluate the absorption onset for these samples and further estimate the band gap. The band gap of the pristine TiO_2 sample was estimated to be 3.2 eV, while the

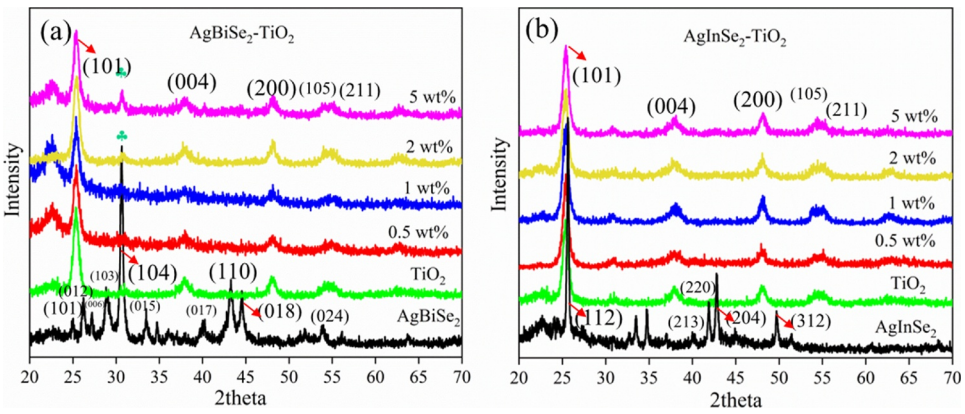

Fig. 5. The XRD patterns of (a) $AgBiSe_2$, $AgBiSe_2$-TiO_2 composites and (b) $AgInSe_2$, $AgInSe_2$-TiO_2 composites.

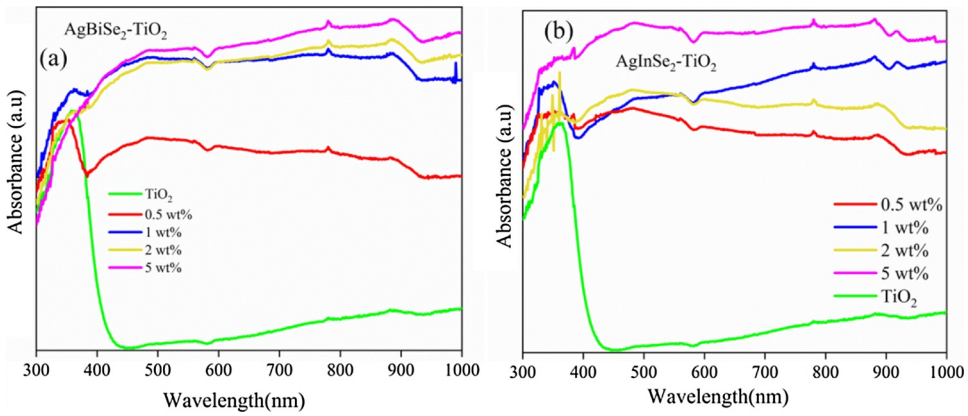

Fig. 6. The absorption patterns of (a) TiO_2, $AgBiSe_2$-TiO_2 composites and (b) TiO_2, $AgInSe_2$-TiO_2 composites.

parent TC samples showed 1.23 eV and 1.33 eV for $AgBiSe_2$ and $AgInSe_2$, respectively. The values obtained are nearly close to the computationally calculated values, as explained in section 3.2. The band gap of the composite samples showed a decline in value with the increase in the content of TC (Figure S9 and S10). Table S2 and Table S3 tabulate the band gap value of all the samples.

The strong interaction of the composite samples results in increased interfacial charge transfer and the decrease in the band gap. The computational analysis of the optical and the electronic properties of the parent samples shows that the band edge of the parent $AgBiSe_2$ is dominated by the contribution of Ag 4*d* and Se 4*p* states. The lower CB of $AgBiSe_2$ is dominated by the combination of Bi 6*p* and Se 4*p* states. While $AgInSe_2$ displayed the contribution of Ag 4*d* states and Se 4*p* states which dominated the upper VB while In 5*s* and Se 4*p* states contributed to the lower CB of $AgInSe_2$. Whereas, TiO_2 displayed a contribution from Ti 3*d*-orbitals in the lower CB while the O 2*p*-orbitals are found to dominate the upper VB. Hence, the composite samples have a combined influence of the parent samples, which is observed experimentally in the enhanced absorption edge as well as the decreased band gap values. This infers the positive hybridisation of the parent samples and construction of heterostructure composites. [25,26] The enhanced absorption properties and in turn, the declined band gap proves to be effective in multifunctional photocatalytic applications (Section 4). The 5 wt% composites of both the TC displayed the best photocatalytic results, as discussed in section 4. Hence, here onward only these two composites are assessed for their morphological and elemental analysis along with their pristine parent samples unless otherwise stated.

3.5. XPS analysis

The elemental states and the chemical composition of the prepared pristine parent and the composite samples were investigated by XPS measurements. The survey scans of TiO_2, $AgBiSe_2$, $AgInSe_2$, $AgInSe_2$-TiO_2 and $AgBiSe_2$-TiO_2 are displayed in Figure S11. Peaks of Ti 2*p* and O 1*s* are found for TiO_2, while $AgInSe_2$ and $AgBiSe_2$ samples displayed common peaks of Ag 3*d* and Se 3*d* and additional peaks of In 3*d* and Bi 4*f* respectively. The composite samples showed all the combined peaks of the parent samples. In all the samples, a small percentage of C 1*s* and O 1*s* peaks were observed, these impurity peaks were acquired during the sample preparation process. To further investigate the charge transfer at the heterojunction interface between TiO_2 and the TC nanoparticles, the high resolution XPS of the composites were also examined. Figure S12(A) displays the Ti 2*p* patterns of TiO_2 (a), $AgBiSe_2$-TiO_2 (b) and $AgInSe_2$-TiO_2 (c). The characteristic peaks at 458.84 eV (Ti $2p_{3/2}$) and 464.60 eV (Ti $2p_{1/2}$), ascribed to Ti^{4+} state was observed for TiO_2 sample. [62] In the case of composite samples, the signature profile of Ti in the +4 state did not show any changes. However, both the doublets of Ti 2*p* in composite samples displayed a small shift in binding energy values. A shift of ~0.3 eV and ~0.4 eV was observed for $AgBiSe_2$-TiO_2 and $AgInSe_2$-TiO_2 respectively. This shift in the composite samples to lower binding energy value compared to the parent sample constitutes the change in the chemical environment of TiO_2 nanoparticles in the due presence of the small amount of TC introduced [25,26]. In all the three samples, the spin-orbit splitting difference for Ti 2*p* remained consistent (5.7 eV). Figure S12(B) displays the deconvoluted O 1*s* patterns of TiO_2 (a), $AgBiSe_2$-TiO_2 (b) and $AgInSe_2$-TiO_2 (c). The characteristic peak at 530.20 eV observed for pristine titania sample is assigned to Ti-O bonds [63]. As similar to the Ti 2*p* patterns, the peaks of O 1*s* also displayed a small shift for the composite sample (~0.3 eV and ~0.4 eV for $AgBiSe_2$-TiO_2 and $AgInSe_2$-TiO_2 respectively). Deconvoluted O 1*s* spectrum also displayed a peak above 531 eV for all the three samples, which is assigned to the hydroxyl molecules adsorbed or the water molecules [64,65].

Fig. 7(A) displays the high-resolution spectra of Ag 3*d* patterns of $AgBiSe_2$ (a) and $AgBiSe_2$-TiO_2 (b). Sharp and symmetric peaks of Ag 3*d* were observed for both the samples. Characteristic peaks of Ag^+ were observed at 367.78 (Ag $3d_{5/2}$) and 373.80 (Ag $3d_{3/2}$) for $AgBiSe_2$ sample. The composite sample with titania displayed a shift (~0.8 eV) in both the peaks to 367.03 (Ag $3d_{5/2}$) and 373.05 (Ag $3d_{3/2}$). The doublet separation remained consistent for the Ag 3*d* patterns for both the samples (6 eV). As shown, Fig. 7(B) displays the deconvoluted high resolution spectra of Bi 4*f* patterns of $AgBiSe_2$ (a) and $AgBiSe_2$-TiO_2 (b). Peaks corresponding to Bi^{3+} state were observed at 159.03 eV (Bi $4f_{7/2}$) and 164.36 eV (Bi $4f_{5/2}$) for $AgBiSe_2$ sample. Moreover, doublets of Bi in the elemental state were also observed in the spectra (157.91 eV and 163.23 eV). In the case of the composite samples, the doublet peaks corresponding to the Bi^{3+} state showed a shift to lower binding energy (~0.6 eV). Apart from that, the peak intensity of elemental Bi reduced and displayed a similar shift in the peak values. In all the cases, the spin-orbit splitting difference of 5.31 eV remained constant. Fig. 7C) displays the deconvoluted high resolution spectra of Se 3*d* patterns of $AgBiSe_2$ (a) and $AgBiSe_2$-TiO_2 (b). Peaks at 53.38 eV (Se $3d_{5/2}$) and 54.27 eV (Se $3d_{3/2}$) were observed for $AgBiSe_2$ sample attributed to Se^{2-} state. The doublet splitting difference was observed to be 0.86 eV, consistent to Se^{2-}. The composite sample did not show any symmetric peaks of Se; however, a small pattern was observed [19,66].

Fig. 8(A) displays the high-resolution spectra of Ag 3*d* patterns of $AgInSe_2$ (a) and $AgInSe_2$-TiO_2 (b). Well defined and symmetric peaks of Ag 3d were observed for both the samples. Characteristic peaks of Ag^+ were observed at 367.70 eV (Ag $3d_{5/2}$) and 373.70 eV (Ag $3d_{3/2}$) for $AgInSe_2$ sample. The composite sample with titania displayed a shift (~0.8 eV) in both the peaks to 366.96 eV (Ag $3d_{5/2}$) and 372.98 eV (Ag $3d_{3/2}$). The doublet separation remained consistent for the Ag 3*d* patterns for both the samples (6 eV). As given, Fig. 8(B) displays the high-resolution spectra of In 3*d*. Signature peaks of In^{3+} state were observed

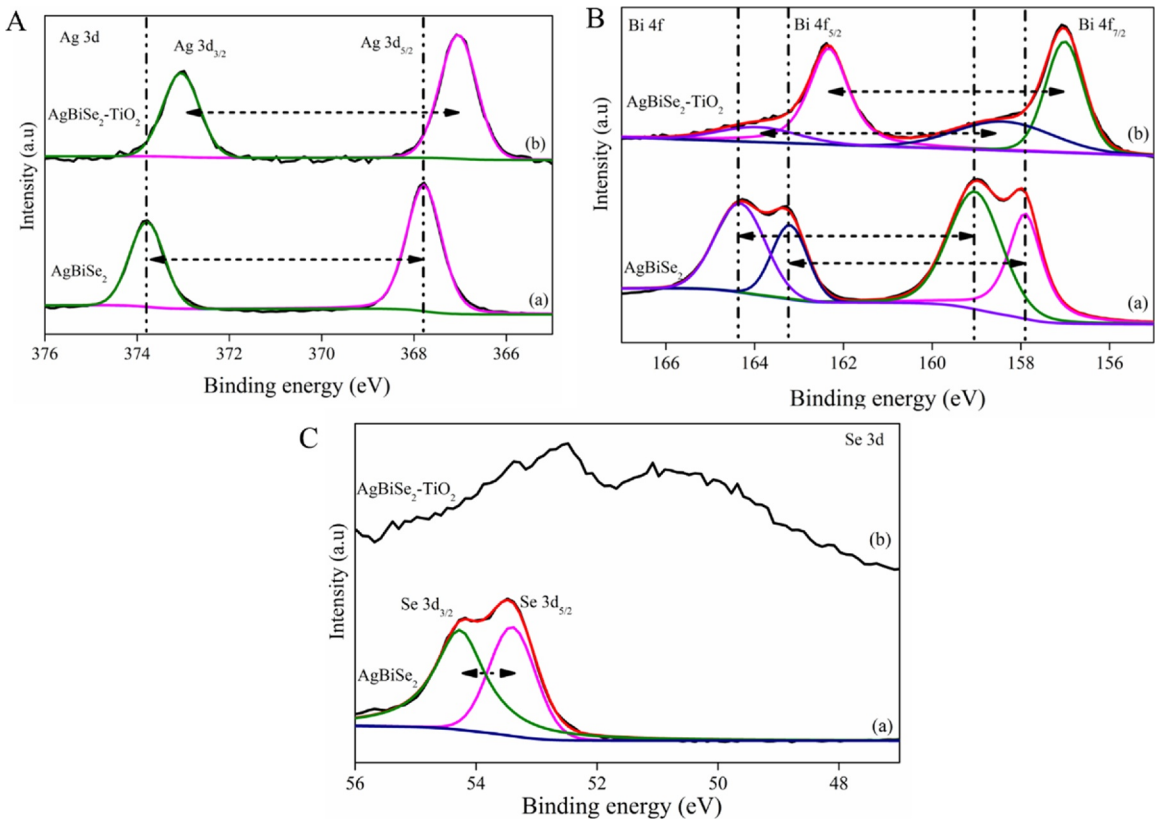

Fig. 7. High resolution XPS spectra of (A) Ag 3*d* (a) $AgBiSe_2$ and (b) $AgBiSe_2$-TiO_2; (B) Bi 4*f* (a) $AgBiSe_2$ and (b) $AgBiSe_2$-TiO_2; (C) Se 3*d* (a) $AgBiSe_2$ and (b) $AgBiSe_2$-TiO_2.

at 444.65 (In $3d_{5/2}$) and 452.24 eV (In$3d_{3/2}$) for $AgInSe_2$ sample. The composite sample, as similar to the other profiles, displayed a shift of ~0.3 eV to lower binding energy value. The spin-orbit splitting difference of 5.31 eV remained the same for both the samples. In case of Se 3*d* patterns, the high-resolution spectra of $AgInSe_2$ sample displayed deconvoluted peaks at 53.67 eV (Se $3d_{5/2}$) and 54.56 eV (Se $3d_{7/2}$) as shown in Fig. 8C(a). The peaks of Se 3d in the composite sample (Fig. 8C(b)) are not so well defined [54,67,68].

Table S4 and S5 summarise the peak position of all the samples. As observed from the above peak patterns were displayed of the pristine parent sample and the composite structures. All the composite patterns displayed a shift in the peak values to lower binding energy values. The change in the chemical environment by the introduction of TC nanoparticles showed the change in the Ti 2*p* and O 1*s* patterns. Similar changes were also observed for pristine $AgBiSe_2$ and $AgInSe_2$ samples. A difference in comparative shift is observed for composite samples between Bi^{3+} (~0.8 eV) while In^{3+} (~0.3 eV) is evident from the spectra. In case of In^{3+} it displays an electronic configuration of [Kr] $4d^{10}$. While Bi^{3+} displays an electronic configuration of [Xe] $4f^{14}$ $5d^{10}$ $6s^2$. The shift in the binding energy, especially to lower energy values signifies the change in the chemical environment due to the effective charge transfer between $AgXSe_2$ and TiO_2 components. The computational study provides an understanding of the density of states. In case of $AgBiSe_2$ the conduction band is dominated by Bi 6*p* orbitals while $AgInSe_2$ shows concentration of In 5*s* orbitals. The move of electrons from the VB to the CB results in the change in the effective nuclear interactions between each of those atoms, which could effectively result in the variation to the shift observed. It crucially varies depending on the combination of element in a ternary chalcogenide molecule. Composites of $AgBiS_2$-TiO_2 and $AgInS_2$-TiO_2 showed similar attribute in the difference between the binding energy shift from the parent sample and the composite sample of Bi^{3+} (~1.1 eV) and In^{3+} (~0.5 eV) spectra was also observed [25,26].

The above-mentioned shift demonstrates the efficient charge transfer at the heterojunction interface and establishes the creation of effective heterostructure for multifunctional applications.

3.6. TEM analysis

Fig. 9a and b show typical TEM images of the as-prepared $AgBiSe_2$ with the particles being nanosheets of average width ranging 50−70 nm. The SAED pattern (Fig. 9c, inset) is consistent with the XRD pattern with the major diffractions of (104), (012), (110) and (018) crystal planes of hexagonal $AgBiSe_2$. Meanwhile, the HRTEM image (Fig. 9c) showed high crystallinity for $AgBiSe_2$ nanocrystals, and the adjacent atomic lattice fringes showed a distance of about 0.293 nm, which is in agreement with the calculated fringe width of 0.291 nm for (104) planes of $AgBiSe_2$ [69]. TEM and HRTEM (Fig. 9d, e, and f) images of 5 wt% $AgBiSe_2$-TiO_2 composite revealed that larger $AgBiSe_2$ particles are covered with smaller titania nanoparticles. HRTEM well matched with fringe width of 0.293 nm corresponding to (104) plane of hexagonal $AgBiSe_2$ for the larger particles in addition to a fringe width of 0.354 nm indicating (101) plane of anatase titania for the smaller particles. SAED pattern (Fig. 9f, inset) again supports the presence of both nanoparticles and is also consistent with XRD obtained.

Fig. 10a and b showed $AgInSe_2$ nanoparticles exposing a quasi-spherical morphology. The HRTEM image (Fig. 10c) showed clear and prominent lattice fringes of 0.34 nm width consistent with the calculated fringe width of 0.346 nm corresponding to (112) crystal plane of tetragonal $AgInSe_2$ (at $2\theta = 25.68^{\circ}$ from XRD). 5 wt% $AgInSe_2$-TiO_2 composite showed nano titania is well accumulated around $AgInSe_2$ having a good interaction between them. The presence of lattice fringe widths of 0.354 nm and 0.235 nm attributing to the (101) crystal planes and (004) planes respectively of anatase titania, along with fringe width of 0.34 nm fitting to (112) plane of tetragonal $AgInSe_2$. Both HRTEM and SAED pattern reflected the high crystallinity of the sample. Both

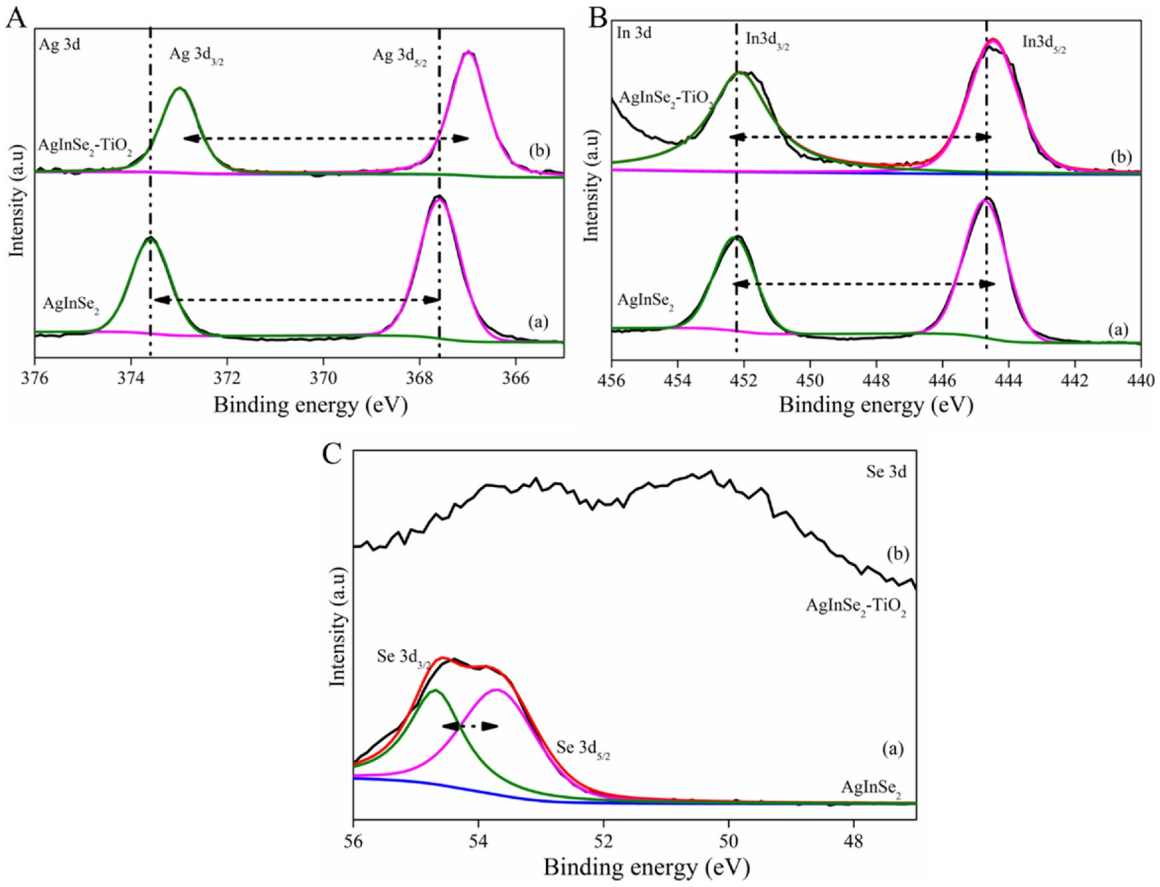

Fig. 8. High resolution XPS spectra of (A) Ag 3*d* (a) $AgInSe_2$ and (b) $AgInSe_2$-TiO_2; (B) In 3*d* (a) $_{AgInSe2}$ and (b) $AgInSe_2$-TiO_2; (C) Se 3*d* (a) $AgInSe_2$ and (b) $AgInSe_2$-TiO_2.

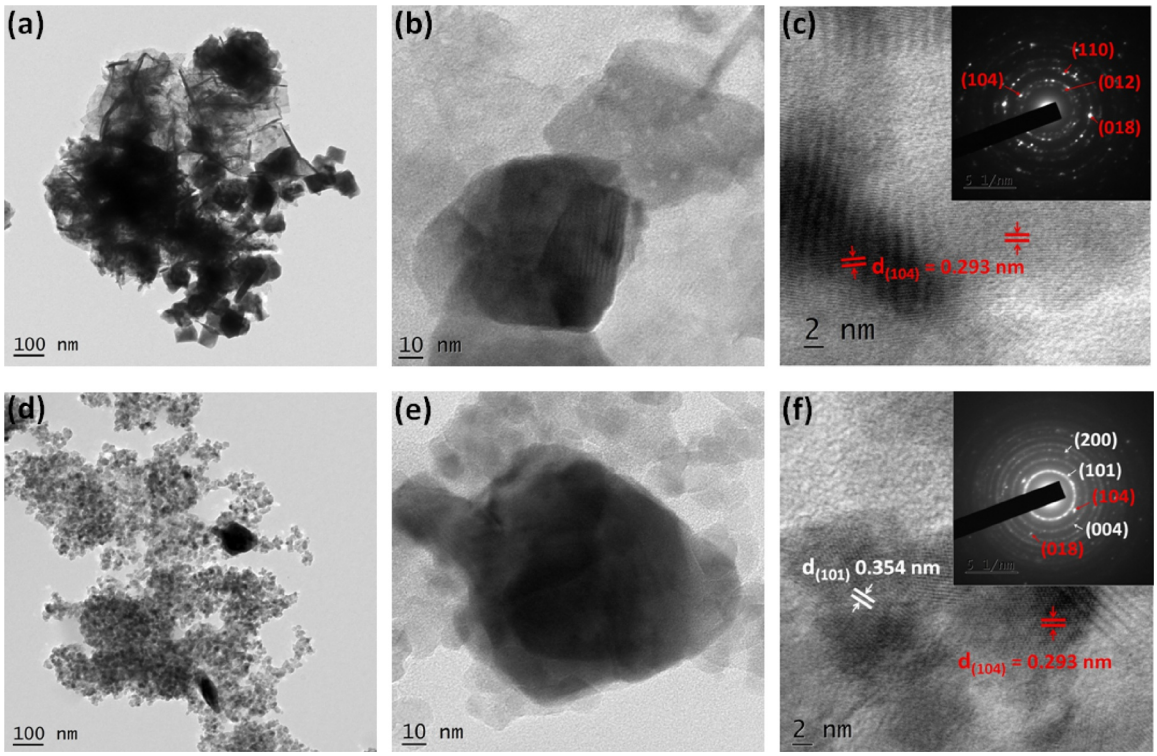

Fig. 9. TEM and HRTEM images of $AgBiSe_2$ (a,b,c) and 5 wt% $AgBiSe_2$-TiO_2 composite (d,e,f). Inset of (c) and (f) are the SAED patterns of the samples with red colour markings corresponding to TC and white to TiO_2.

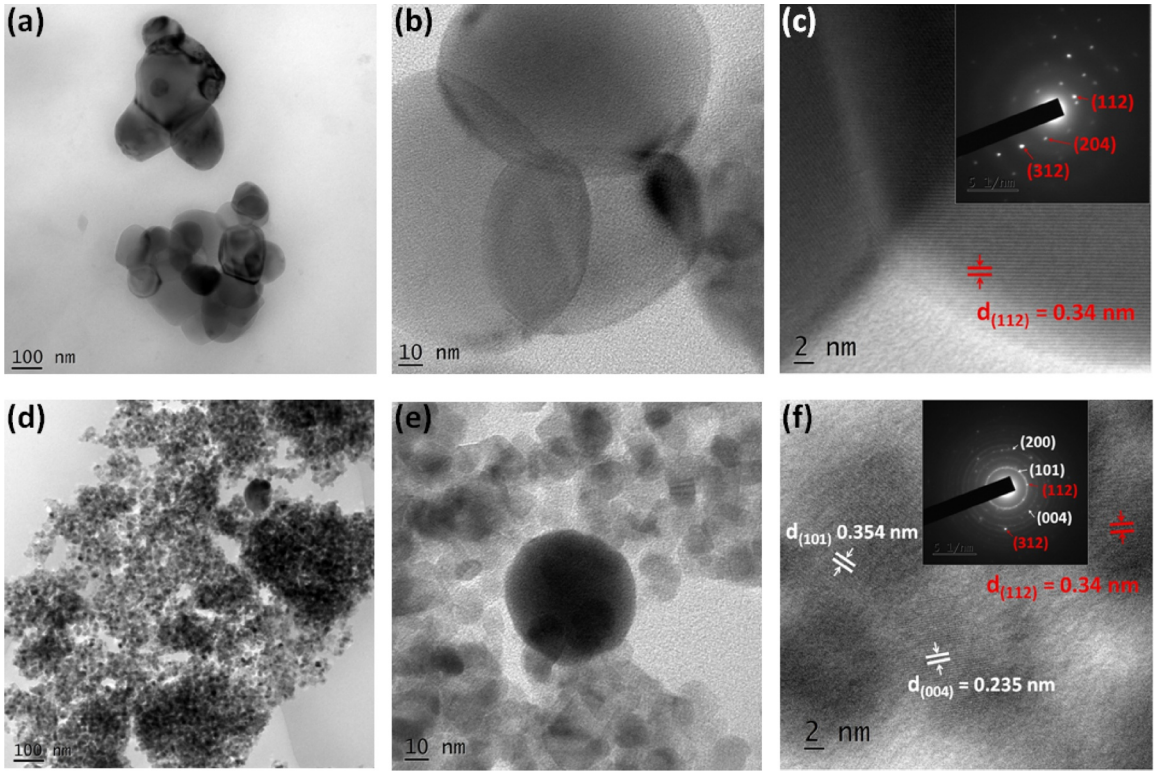

Fig. 10. TEM and HRTEM images of $AgInSe_2$ (a,b,c) and 5 wt% $AgBiSe_2$-TiO_2 composite (d,e,f). Inset of (c) and (f) are the SAED patterns of the samples with red colour markings corresponding to TC and white to TiO_2.

SAED patterns of $AgInSe_2$ and the composite (Fig. 10c and f, inset) obtained are again consistent with the XRD pattern of the samples.

3.7. Photoluminescence analysis

The photocatalytic efficacy is largely governed by the ability of the composite structure to migrate the photogenerated exciton to various reaction sites. [70] Figure S13 presents the mass normalized photoluminescence spectra of TiO_2 and its 5 wt% composites with $AgBiSe_2$ and $AgInSe_2$. The spectra clearly portray the effect of heterojunction formation on the recombination of excitons in parent TiO_2. The emission intensity of both composites of TCs with TiO_2 is quenched. Since PL emission has resulted from the recombination of photogenerated electron-hole pairs, the reduction in the PL intensity for the composites indicates that recombination rate is very much diminished, resulting in their high photocatalytic efficiencies compared to parent TiO_2. The emission peaks at 365 nm displayed a small red shift in the composite samples compared to the pristine parent sample. This is attributed to the change in the local chemical environment of the sample and this further validates the positive heterojunction creation [71].

4. Photocatalytic applications

4.1. Photocatalytic hydrogen generation

Hydrogen is considered as a clean source of fuel having heat value 120–142 MJ kg^{-1} [72]. There exist several methods currently used to produce hydrogen such as thermolysis, photolysis, hydrolysis *etc* [72]. The use of photocatalysis for H_2 generation is a promising alternative to accomplish the global need for clean energy. In this following section, the results of photocatalytic hydrogen generated for $AgBiSe_2$-TiO_2 and $AgInSe_2$-TiO_2 was examined at different weight percentage and compared to the results observed for their parent samples. In particular, the possibility to adapt the materials prepared to produce hydrogen through the photocatalytic reforming of an organic species was examined.

As shown in Fig. 11a, no catalyst revealed hydrogen generation under visible light irradiation (first 60 min of reaction). After 60 min, by removing the UVA-cut off filter, an increasing value of hydrogen production rate for the $AgBiSe_2$-TiO_2 materials was observed with raising the co-catalyst weight percentage up to 5 wt %. No hydrogen production was detected at all by adopting bare $AgBiSe_2$ and TiO_2 samples.

As reported in Fig. 11b, no substantial changes in solution pH were recorded for the $AgBiSe_2$-TiO_2 samples throughout the reaction, with an average value of 8.5. A slight decrease in pH was observed upon UV-A irradiation, due to the occurrence of the photoreforming process.

In the first 60 min of reaction, the irradiance values (Fig. 11c) recorded in the UV range (λ = 315-400 nm) on the external wall of the reactor were negligible due to the UVA-cut off filter. An immediate increase in the irradiance values was detected after removing the UVA-cut off filter. A slight decrease in irradiances was then observed at T = 120 min, due a higher suspension absorption related to photocatalyst activation. As concerns irradiance values collected on the external walls of the reactor in the visible range (λ = 400-1100 nm), no significant changes before and after removing the UVA-cut off filter were observed, as clearly shown in Fig. 11d. Even in this case, a mild decrease in irradiances was observed at T = 120 min.

Also, in the case of $AgInSe_2$-TiO_2, as shown in Fig. 12a, all the catalyst tested displayed negligible hydrogen production under UV light irradiation only. As the UV cut-off filter was removed (T = 60 min), increasing hydrogen production was observed with enhancing the co-catalyst weight percentage in the range 1%–5%. Scarce photoactivity for hydrogen evolution was recorded upon UV-A irradiation of the 0.5 wt.% $AgInSe_2$-TiO_2 composite. As regards to the solution, no significant changes concerning the starting pH values were recorded under visible light irradiation only (Fig. 12b). A moderate decrease in solution pH occurred upon UV-A irradiation of $AgInSe_2$-TiO_2 samples at T = 120

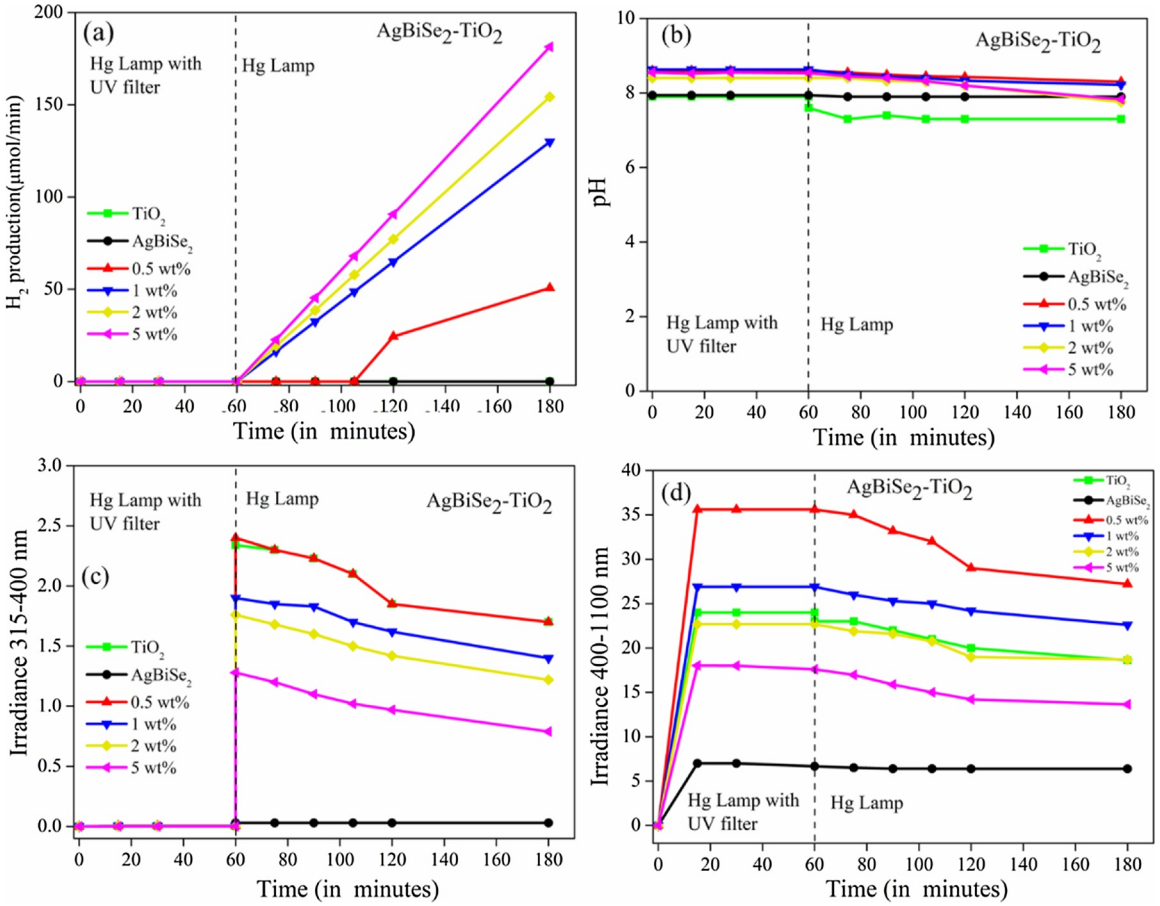

Fig. 11. H_2 production rate (a); pH of the solution (b); Irradiance measured on the external walls of the reactor between 315-400 nm (c) and 400-1100 nm (d) at varying weight percentage of $AgBiSe_2$, TiO_2 and $AgBiSe_2$-TiO_2 catalysts. [CH_3OH] = 10 vol.%; Catalyst load = 500 ppm; Temp = 25 °C; P = 1 atm.

min.

The irradiance values collected in the UV and the visible wavelength range on the external wall of the reactor for the various the $AgInSe_2$-TiO_2 samples tested are reported in Fig. 12c and d, respectively. An instantaneous increase in UV irradiance values was observed after removing the UVA-cut off filter. The higher irradiance values herein recorded for the 0.5 wt% $AgInSe_2$-TiO_2 material suggest a smaller suspension absorption. As regards irradiance values collected on the external walls of the reactor in the visible range (λ = 400-1100 nm), no significant changes before and after removing the UVA-cut off filter were noticed. Comparable irradiance values have been recorded in such range for 2 wt% and 5 wt% $AgInSe_2$-TiO_2 samples, which exhibited a higher visible light absorption with respect to samples with lower co-catalyst percentage.

Thus, both the composites displayed a relative hydrogen generation compared to their parent samples within 120 min of light irradiation. It can be thus concluded that both $AgBiSe_2$-TiO_2 and $AgInSe_2$-TiO_2 materials exhibited a more efficient absorption and use of the incident light irradiation over a co-catalyst weight percentage of 5 wt.%. However, $AgInSe_2$-TiO_2 (241 μmol/min) composites outperformed the $AgBiSe_2$-TiO_2(180 μmol/min) in a slight margin. While all the pristine samples displayed no hydrogen output. As explained in section 3.2, the band edge estimation displays the potential for HER and OER only for TiO_2 and $AgInSe_2$, while $AgBiSe_2$ did not display any significant potential. However, the quick recombination and the values of the band gap could be the potential causes for zero hydrogen generation. On the other hand, both the composite samples displayed enhanced H_2 generation, which portrays the significance of the heterojunction creation and the enhanced charge separation by delaying the rate of recombination [73].

4.2. Photocatalytic degradation of Doxycycline (DC)

Further, to the hydrogen generation study, the composites of $AgXSe_2$-TiO_2 were examined for Doxycycline degradation. Antibiotics such as Doxycycline are one of the major pharmaceutical products used widely. The estimated annual consumption of antibiotics is 100,000–200,000 tons. Amongst which 30%–60% is expelled out in the environment, due to incomplete metabolism. A good share of the expelled antibiotics leads its way to pollute several water resources. Long term exposure to even small measures of antibiotics, could eventually result in the development of antibiotics resistance and even cause damage to the nervous system and the kidneys of the human body. Advanced oxidation processes (AOP), biological degradation and membrane filtration are some of the commonly utilised methods of DC removal. Photocatalytic degradation has lately turned out to be an effective alternative to alleviate the current problem [74,75].

Hence, in this study, the composites of $AgBiSe_2$-TiO_2 and $AgInSe_2$-TiO_2 were examined for DC degradation at different weight percentage and compared to the results observed for their parent samples. Fig. 13a displays the change in concentration of DC with time for $AgBiSe_2$-TiO_2 samples. The samples kept in the dark for 30 min did not show any change in concentration; this proves the significance of light irradiation. On exposure to solar light for a period of 180 min, samples displayed a significant reduction in the initial concentration of DC by the composite samples. Parent samples, TiO_2 and $AgBiSe_2$, displayed a degradation percent less than 50 %. The increase in the loading of TC in TiO_2 showed gradual improvement in the degradation process. Towards the end, the 2 wt% and the 5 wt% samples displayed a nearly similar trend of 98 % degradation. Hence, this proves the efficiency of the composite formation and the enhanced charge separation built up.

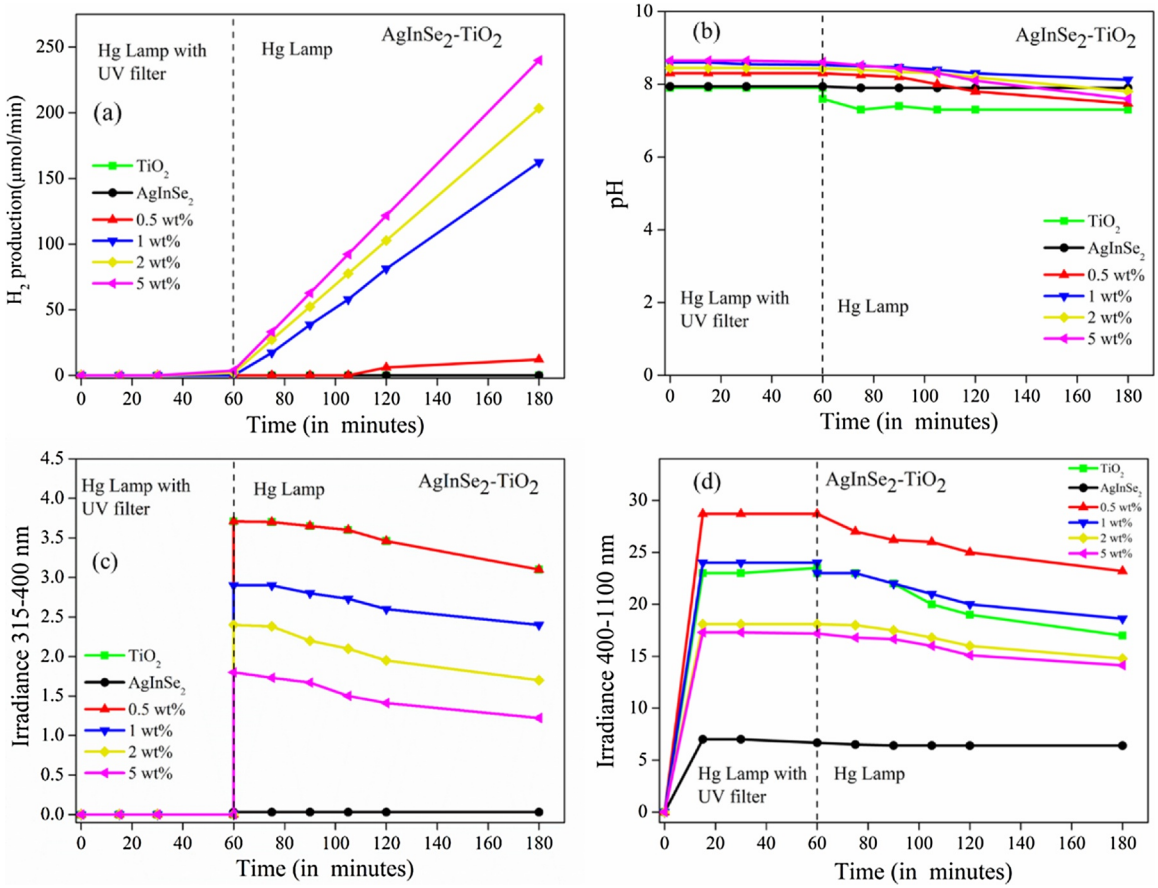

Fig. 12. H_2 production rate (a); pH of the solution (b); Irradiance measured on the external walls of the reactor between 315-400 nm (c) and 400-1100 nm (d) at varying weight percentage of $AgInSe_2$, TiO_2 and $AgInSe_2$-TiO_2 catalysts. [CH_3OH] = 10 vol.%; Catalyst load = 500 ppm; Temp = 25 °C; P = 1 atm.

The DC degradation of $AgBiSe_2$-TiO_2 samples observed to follow pseudo-first-order kinetics and can be determined by Eq. (9) [61].

$$Log\frac{C_0}{C_t} = kt \tag{9}$$

Where C_0 and C_t are the DC concentration (mg/L) at time zero and time '*t*' respectively. '*k*' in the equation is the kinetic rate constant (min^{-1}). Fig. 13b and c illustrate the kinetics for the DC degradation and summarise the kinetic constants calculated for all the samples respectively. A straight line was observed for all the cases, and this confirms the presumed pseudo-first-order kinetics. The correlation coefficients (R^2) values for all the samples were found to be more than 0.98. The highest kinetic constant for 5 wt % was observed to be 0.02663 min^{-1}, and the least was observed for $AgBiSe_2$ (0.00316 min^{-1}).

The recyclability of the catalyst and its effectiveness was evaluated through the cyclic studies (Figure S14a). The 5 wt% composite samples displayed similar results all the time with a slight decline in the degradation efficiency by the end of the fifth cycle. To ascertain the reactive oxygen species (ROS) participating in the degradation process, the scavenging experiments were performed (Figure S14b). The use of triethanolamine (TEA) and Silver nitrate ($AgNO_3$) showed a serious dampening in the degradation efficiency. Thus, holes and electrons were found to be the major ROS in the DC degradation process. On the other hand, a small portion of the decline in activity was observed in the presence of benzoquinone (BQ). Thus, superoxide radicals also had an effective share in the degradation process. The hydroxyl radicals necessarily did not show any contribution, as observed by the addition of the Isopropyl alcohol (IPA) in the reaction mixture.

The composites of $AgInSe_2$-TiO_2 were also examined for DC degradation at different weight percentage and compared to the results observed for their parent samples. Fig. 14 a displays the change in concentration of DC with time for $AgInSe_2$-TiO_2 samples. In this case, also, the samples kept in the dark for 30 min did not show any variation in concentration; this reflects the consequence of light irradiation. Under solar light irradiation for 180 min showed a substantial decrease in the initial concentration of DC by the composite samples. Parent samples, TiO_2 and $AgInSe_2$, showed a degradation percent less than 50 %. As similar to the previous case, the increase in the amount of TC in TiO_2 presented steady improvement in the degradation method. In the end, the 2 wt% and the 5 wt% samples exhibited a virtually similar trend of more than 92 % degradation. Henceforth, this demonstrates the efficacy of the composite development and the improved charge separation created.

The DC degradation of $AgInSe_2$-TiO_2 samples also observed to follow pseudo-first-order kinetics and can be determined by Eq. (9). Fig. 14b and c show the kinetics for the DC degradation and reviews the kinetic constants calculated for all the samples respectively. The presumed pseudo-first-order kinetics was confirmed by observing the straight line for all the cases. The correlation coefficients (R^2) values for all the samples were found to be more than 0.97. The maximum kinetic constant for 5 wt % was calculated to be 0.02643 min^{-1} and the minimum was observed for $AgInSe_2$ (0.00317 min^{-1}).

The cyclic studies of the catalyst were performed to evaluate the recyclability and its effectiveness (Figure S15a). The 5 wt% composite samples showed comparable results all the time with a small decrease in the degradation efficacy by the end of the fifth cycle. The scavenging experiments were performed, with the purpose to ascertain the ROS contributing to the degradation procedure (Figure S15b). The use of triethanolamine and silver nitrate showed a quick reduction in the degradation efficacy; thus, holes and electrons were found to be the

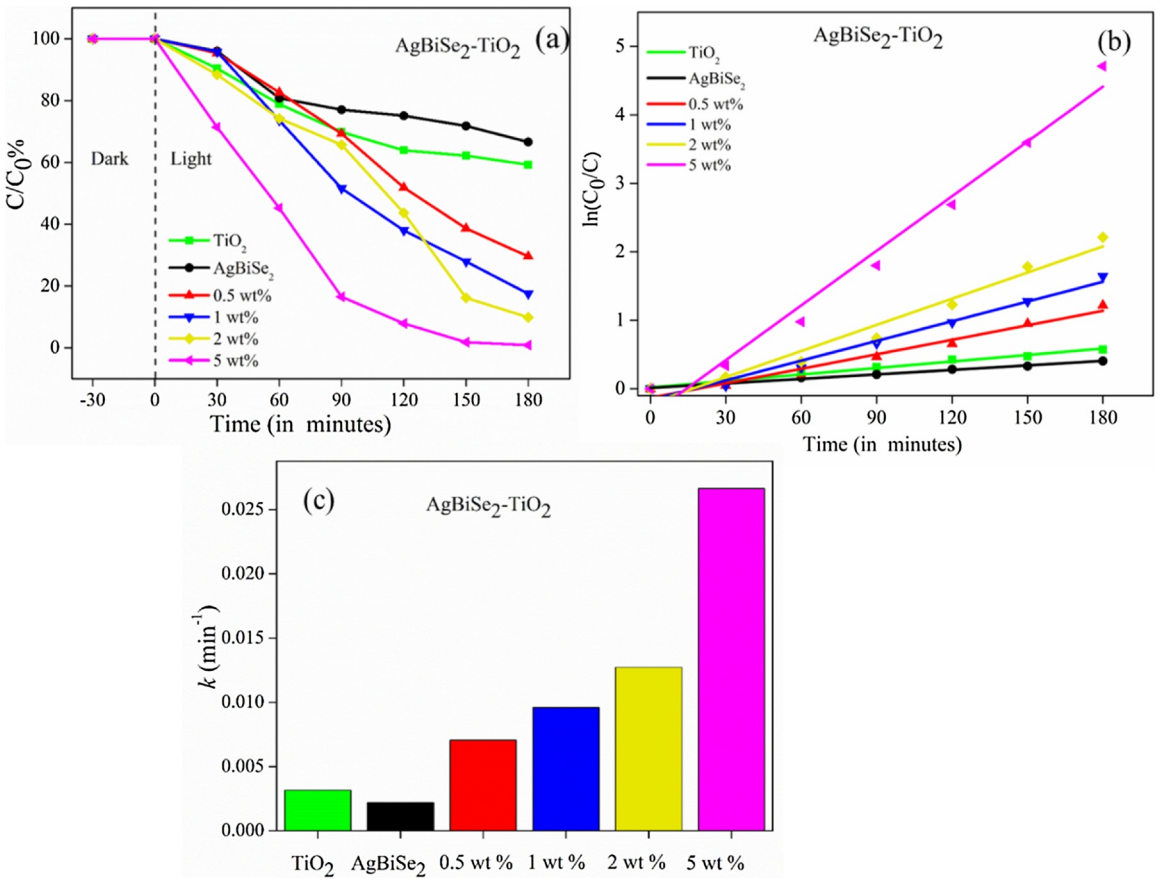

Fig. 13. (a) Change in concentration (C/C_0 vs time) of DC; (b) pseudo-first-order kinetic study of DC degradation; (c) Summary of the calculated pseudo-first-order rate constants of $AgBiSe_2$, TiO_2 and $AgBiSe_2$-TiO_2 catalysts.

major ROS in the DC degradation process. Instead, a small portion of decay in activity was observed in the presence of benzoquinone. Therefore, superoxide radicals also had an active part in the degradation process. The hydroxyl radicals essentially did not demonstrate any influence, as detected by the adding of the IPA in the reaction mixture [25].

Hence, in this study of DC removal from aqueous environment, both the composites of titania displayed reasonable efficiency. According to the results observed, the 5 wt% composites of both the TC displayed more than 98 % decline of initial DC concentration of 100 ppm for a catalyst dosage of 1 g/L. Pseudo-first order kinetics was observed for both the composites ($R^2 > 0.98$) with the highest rate constant of 0.026 min^{-1}. The efficiency did not change as observed through the recyclability and the stability test and therefore, the catalyst might be used regularly based on its possible retrieval. Thus, this catalyst could be suitable for demineralisation of persistent pharmaceutical organic pollutants.

4.3. Photocatalytic antimicrobial disinfection

Drinking of contaminated water results to the death of 1.5 million children of age under five worldwide. The presence of *E. coli* and *S. aureus* are considered as an index for water quality. Microbially contaminated water could result in the cause of several infections and even death. Typical water treatment procedures include ozonation, UV disinfection technique, chlorination *etc*. These methods have displayed several disadvantages, such as secondary contamination from the microorganisms left, even after primary treatments. Disadvantages of chlorination processes are not new, as the formation of carcinogens like trihalomethanes is reported widely. Thus, it is indeed necessary to find effective microbial inactivation processes [74,75].

Titania and its composites have extensively been reported for self-cleaning and degradation activities of several organic contaminants. Extensive studies on the photoinactivation of microorganisms by TiO_2 has been reported recently. The photocatalytic efficiency of the as prepared composites was already analysed by studying for hydrogen generation and DC degradation. In this study, a gram-negative (*E. coli*) and a gram-positive (*S. aureus*) bacterium were chosen as a model microorganism to evaluate the efficacy of the composites and compare their results with their parent samples. The best composite samples from the previous two applications (5 wt%) and the pristine samples of $AgBiSe_2$, $AgInSe_2$, TiO_2 were studied. Fig. 15a and b display the change in the number of bacteria grown over 120 min of light irradiation. The dark experiment conducted displayed no change in the numbers; this limit the possibility of dark inactivation caused due to the presence of a catalyst. In the case of *E. coli* inactivation, complete death of the bacteria was observed within 45 min of solar light illumination by $AgBiSe_2$-TiO_2 composite. A similar result was also displayed in the case of *S. aureus*, where all the colonies cease to exist. An approximate log 6 and log 5 reduction in bacterial growth was observed in the case of $AgBiSe_2$-TiO_2 composite (Fig. 15c). The $AgInSe_2$-TiO_2 composite and TiO_2, both showed a complete inactivation within 60 min of illumination. The pristine TC samples required nearly 120 min to display complete inactivation. The change in bacterial density grown on agar plates before and after illumination with $AgBiSe_2$-TiO_2 and $AgInSe_2$-TiO_2 composite for both the bacterial strains are displayed in Fig. S16 and Fig. S17, respectively.

Thus, both the composites of TC displayed a similar result; however, $AgBiSe_2$-TiO_2 composites displayed superior inactivation performance. The bacterial inactivation mechanism is established in previous other literature. Disruption of the cellular membrane due to potential attack by ROS generated during the irradiation process results in the leakage

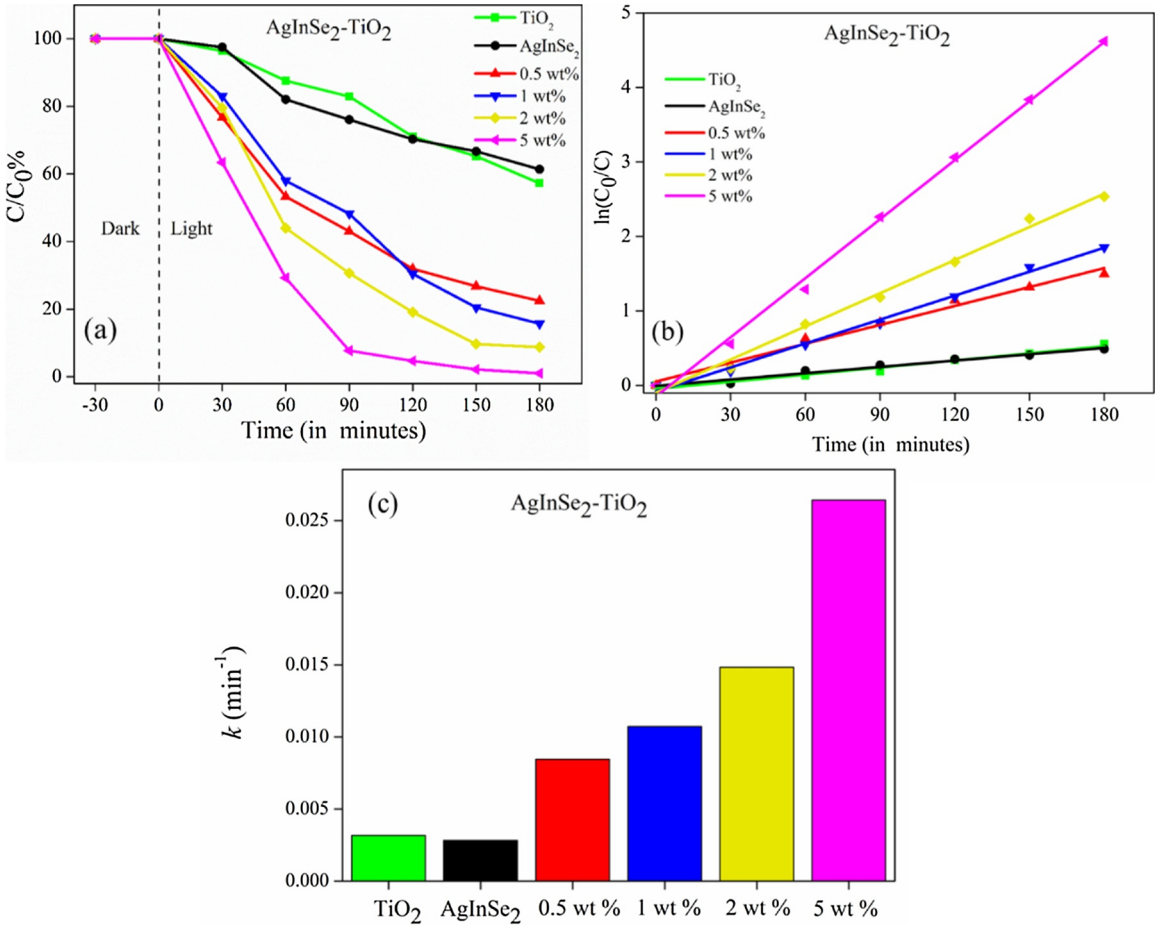

Fig. 14. (a) Change in concentration (C/C_0 vs time) of DC; (b) pseudo-first order kinetic study of DC degradation; (c) Summary of the calculated pseudo-first order rate constants of $AgInSe_2$, TiO_2 and $AgInSe_2$-TiO_2 catalysts.

of cellular components and results to the cause of inactivation [3].

5. Photocatalytic mechanism

The photocatalytic results of the $AgXSe_2$-TiO_2 displayed enhanced hydrogen generation, impressive degradation efficiency as well as antimicrobial properties compared to their pristine parent samples. The structural analysis displays the stability of the hexagonal phase of $AgBiSe_2$ and the tetragonal crystal structure of anatase and $AgInSe_2$, which corroborated to the experimental observations. The computational analysis of titania and TC were crucial to comprehend the electronic and optical properties. The results from XPS analysis demonstrates the shift in the binding energies of both the composite structures to lower energies. This highlights the strong interaction between the pristine titania and TC. On the other hand, the peaks corresponding to Ti^{4+} state displayed a small shift to lower binding energy, which is ascribed to the influence of TC. The peak value also confirms the absence of any oxygen vacancies and reiterates the anatase structure and positive heterojunction formation. The TEM analysis also displayed a positive heterojunction creation. At the same time, the PL emission peaks displayed the delayed recombination by the composite samples. The band gap estimation and the electronic properties aided in summarising the band edge values for $AgBiSe_2$, $AgInSe_2$ and TiO_2 (as given in Table S1). A prospective electron-transfer mechanism is proposed based on the computational, DRS and PL observations in order to understand the improved photocatalytic results displayed by the composites architectures.

Visible light irradiation on $AgBiSe_2$-TiO_2 composites results in the electrons to jump from the upper VB of Ag 4*d* and Se 4*p* states to the lower CB of Bi 6*p* and Se 4*p* states of $AgBiSe_2$ respectively and further travel to the O 2*p*-orbitals of titania. The improved photocatalytic activity by the $AgBiSe_2$-TiO_2 composites could be described *via* conjecturing the formation of *p-n* heterojunction [76,77]. The band edge positions of TiO_2 and $AgBiSe_2$ before and after having contact are shown in Fig. 16. The Fermi level (E_f) of *n*-type TiO_2 is present slightly below the E_{CB} of TiO_2, and the E_f of *p*-type $AgBiSe_2$ is slightly higher than the E_{VB} of $AgBiSe_2$ (Fig. 16a) [65,66]. As the *p-n* junction is created, the Fermi levels of both the semiconductors align themselves to a new uniform level. Since the dopant amount in case of $AgBiSe_2$ is low, therefore the fermi level of $AgBiSe_2$ bring into line with TiO_2 (-0.1 eV). This results in the formation of *p-n* heterojunction in the interface. The new band alignment as shown in Fig. 16b displays the flow of the electrons present in the CB potential of $AgBiSe_2$, transfers to the more negative CB of TiO_2 resulting in a negative charge accumulation in the CB of TiO_2. Similarly, the diffusion of the holes from the VB of TiO_2 to the VB of $AgBiSe_2$ results in positive charge accumulation. Hence, the equilibration of the fermi levels of both the semiconductors results in the creation of an internal electric field [61]. Therefore, the resultant electric field prohibits the charge recombination in the junction and thereby improving the charge separation. The electrons and holes accumulated at the VB of $AgBiSe_2$ and CB of TiO_2 respectively participate in the oxidation and reduction processes [76,77]. The scavenging results, as shown in section 4.2, shows the contribution of both electrons and holes to be dominant, which explains the improved photocatalytic results observed for all the three different applications.

Similarly, in the case of $AgInSe_2$-TiO_2 composites, the visible light illumination results in the migration of electrons to occur from the upper VB of Ag 4*d* states and Se 4*p* states of $AgInSe_2$ to the lower CB of

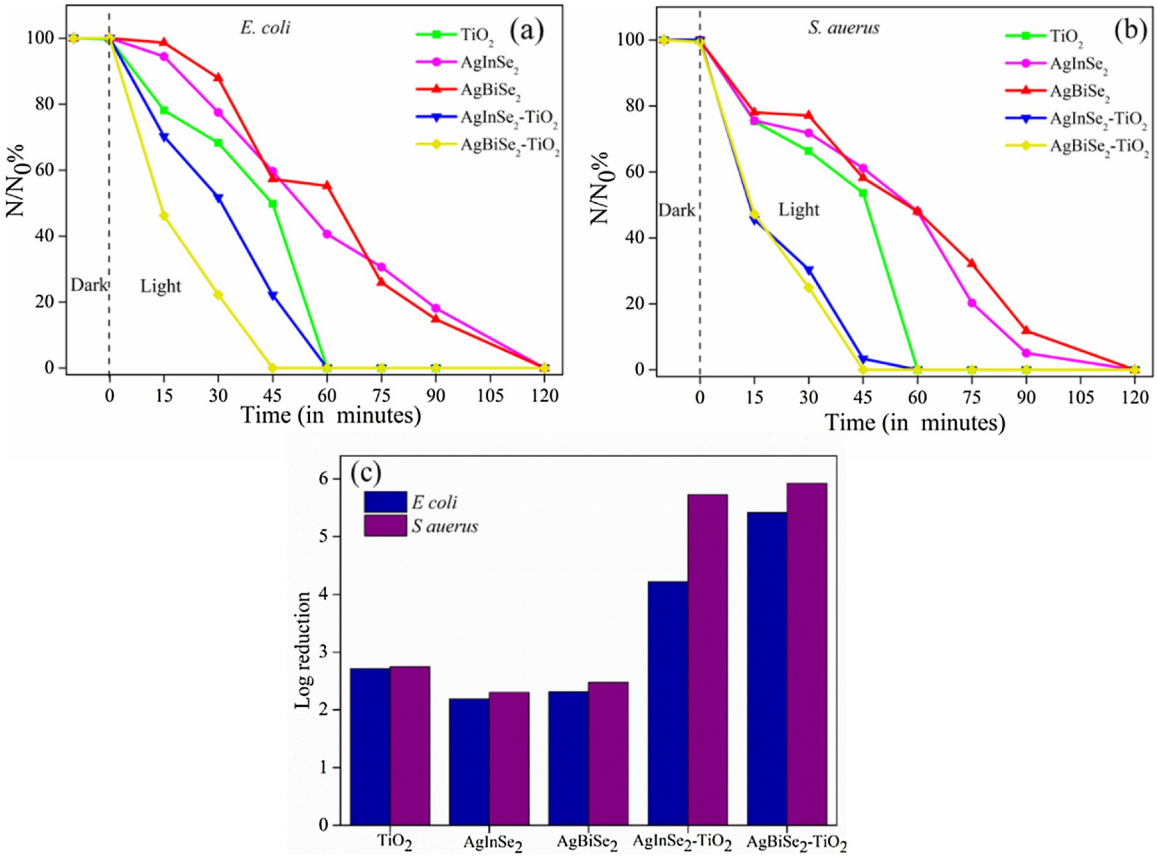

Fig. 15. Change in bacterial density (N/N_0 vs time) by photocatalytic inactivation of (a) *E. coli* and (b) *S. aureus*; and (c) calculated log reductions of $AgBiSe_2$, $AgInSe_2$, TiO_2 and $AgBiSe_2$-TiO_2, $AgInSe_2$-TiO_2 catalysts.

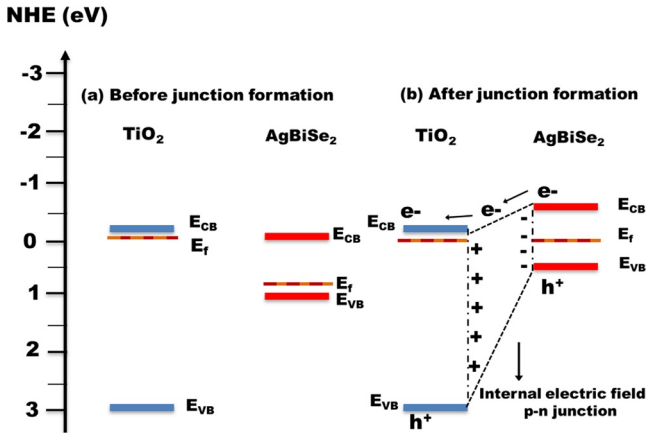

Fig. 16. a) Band alignment of *p*-type $AgBiSe_2$ and *n*-type TiO_2 before junction formation and b) band alignment and the photocatalytic mechanism of $AgBiSe_2$-TiO_2 *p–n* nano-heterojunctions.

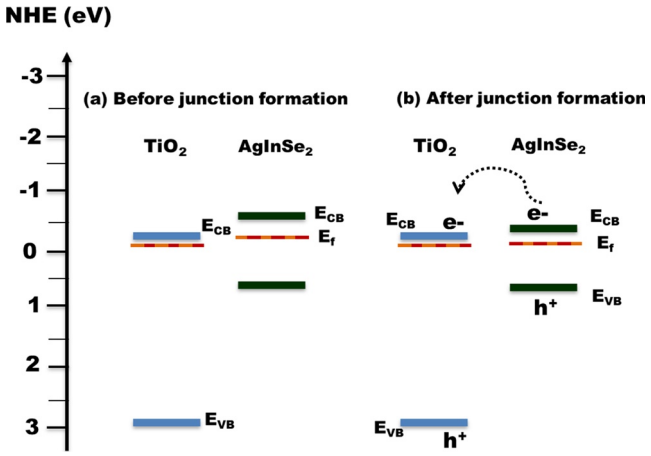

Fig. 17. The photocatalytic mechanism for $AgInSe_2$-TiO_2.

In 5*s* and Se 4*p* states of $AgInSe_2$ and further migrate to the lower CB of titania contributed by Ti 3*d*-orbitals O 2*p*-orbitals. The improved photocatalytic activity by the $AgInSe_2$-TiO_2 composites could be defined *via* hypothesising the formation of type II heterojunction. The band edge positions of TiO_2 and $AgInSe_2$ before and after having contact are shown in Fig. 17. The Fermi level (E_f) of TiO_2 is present slightly below the E_{CB} of TiO_2, and the E_f of $AgInSe_2$ is also lower than the E_{CB} of $AgInSe_2$ (Fig. 17a). As the heterojunction is created, the Fermi levels of both the semiconductors align themselves to a new uniform level. Since the dopant amount in case of $AgInSe_2$ is little, therefore the fermi level of $AgInSe_2$ bring into line with TiO_2 (-0.1 eV). The new band alignment, as shown in Fig. 17b, displays the flow of the electrons from the CB potential of $AgInSe_2$ to the CB of TiO_2, resulting in a negative charge accumulation in the CB of TiO_2. The diffusion of the holes from the VB of TiO_2 to the VB of $AgInSe_2$, which results in positive charge accumulation. The heterojunction creation results in the delayed charge recombination in the junction and thereby improving the charge separation. The electrons and holes accumulated at the CB of TiO_2 and VB of $AgInSe_2$ respectively participate in the oxidation and reduction processes. The experimental results of the scavenging process, as shown in section 4.2, displays the contribution of both the electrons and the holes for the improved photocatalytic results observed for all the three different applications.

Hence, the above electron transfer mechanism emphasises the

influence of the lattice forming element in the ternary combination of chalcogenides. The *p-n* heterojunction and the type II configuration observed for $AgBiSe_2$-TiO_2 and $AgInSe_2$-TiO_2, respectively helps in explaining the increased efficiency observed for the composite samples.

6. Conclusions

The present study successfully demonstrates the synthesis of composites of $AgBiSe_2$-TiO_2 and $AgInSe_2$-TiO_2. The influence of the lattice forming elements (In/Bi) is extremely crucial. As observed in this study, the In^{3+} and Bi^{3+} cations result in the formation of the body-centred tetragonal crystal structure of $AgInSe_2$ and hexagonal crystal structure of $AgBiSe_2$, respectively. The electronic properties of both the structures show a significant influence of the In and Bi orbitals. An indirect band gap was estimated for TiO_2 and $AgBiSe_2$ while direct band gap was observed for $AgInSe_2$. However, both the synthesised nanoparticles displayed a narrow band gap and effectively improved the visible light absorption of the composite architectures. The TEM images displayed the formation of heterojunction and the PL peaks corroborated the delayed recombination, observed for the composite samples compared to the pristine titania. The band alignment of $AgBiSe_2$ and $AgInSe_2$ displayed a very different variation. However, both the heterojunctions result in effective charge separation *via* delayed recombination of the charge carriers, which contributes to the enhanced photocatalytic results.

Credit author statement

Priyanka Ganguly: Conceptualization, Methodology, Writing-Original draft preparation

Syam Kumar R and A. Akande: DFT calculations, Data curation.

Ailish Breen and Suresh C. Pillai: Supervision, Reviewing and Editing,

Steven Hinder: XPS Analysis

Snehamol Mathew: Anti-bacterial Studies

Nisha T. Padmanabhan and Honey John: TEM Studies

Marica Muscetta, Laura Clarizia; Hydrogen production studies.

Declaration of Competing Interest

The authors declare that they have no known competing financial interests or personal relationships that could have appeared to influence the work reported in this paper.

Acknowledgements

PG and SK would like to acknowledge the Institute of Technology Sligo President's Bursaryfor providing financial support (grant no: PPRES052 andPPRES050respectively). Computational resources have been provided by the supercomputer facilities at the Trinity Centre for High Performance Computing (TCHPC) under the project code: HPC_16_00953 and Irish Centre for High-End Computing (ICHEC) under the project codes: is-phy002c and is-phy003c. PG would like to acknowledge Dr. Manu Jose for the JCPDS files. SCP and SM would like to thank the European Union's INTERREG VA Programme for the Renewable Engine (RE) project, managed by the Special EU Programmes Body (SEUPB), with match funding provided by the Department for the Economy and Department of Jobs, Enterprise and Innovation in Ireland

Appendix A. Supplementary data

Supplementary material related to this article can be found, in the online version, at doi:https://doi.org/10.1016/j.apcatb.2020.119612.

References

[1] R. Georgekutty, M.K. Seery, S.C. Pillai, A highly efficient Ag-ZnO photocatalyst: synthesis, properties, and mechanism, J. Phys. Chem. C 112 (2008) 13563–13570.
[2] V. Etacheri, M.K. Seery, S.J. Hinder, S.C. Pillai, Oxygen rich titania: A dopant free, high temperature stable, and visible-light active anatase photocatalyst, Adv. Funct. Mater. 21 (2011) 3744–3752.
[3] P. Ganguly, C. Byrne, A. Breen, S.C. Pillai, Antimicrobial activity of photocatalysts: fundamentals, mechanisms, kinetics and recent advances, Appl. Catal. B: Environ. 225 (2018) (2017) 51–75.
[4] H. Huang, J. Feng, S. Zhang, H. Zhang, X. Wang, T. Yu, C. Chen, Z. Yi, J. Ye, Z. Li, Molecular-level understanding of the deactivation pathways during methanol photo-reforming on Pt-decorated TiO2, Appl. Catal. B: Environ. (2020) 118980.
[5] J. Fu, Q. Xu, J. Low, C. Jiang, J. Yu, Ultrathin 2D/2D WO3/g-C3N4 step-scheme H2-production photocatalyst, Appl. Catal. B: Environ. 243 (2019) 556–565.
[6] Y. Zhang, Z. Huang, J. Shi, X. Guan, C. Cheng, S. Zong, Y. Huangfu, L. Ma, L. Guo, Maleic hydrazide-based molecule doping in three-dimensional lettuce-like graphite carbon nitride towards highly efficient photocatalytic hydrogen evolution, Appl. Catal. B: Environ. (2020) 119009.
[7] A. Sahu, L. Qi, M.S. Kang, D. Deng, D.J. Norris, Facile synthesis of silver chalcogenide (Ag2E; E= Se, S, Te) semiconductor nanocrystals, J. Am. Chem. Soc. 133 (2011) 6509–6512.
[8] D. Yao, H. Liu, Y. Liu, C. Dong, K. Zhang, Y. Sheng, J. Cui, H. Zhang, B. Yang, Phosphine-free synthesis of Ag–In–Se alloy nanocrystals with visible emissions, Nanoscale 7 (2015) 18570–18578.
[9] O.S. Oluwafemi, B.M. May, S. Parani, N. Tsolekile, Facile, large scale synthesis of water soluble AgInSe2/ZnSe quantum dots and its cell viability assessment on different cell lines, Mater. Sci. Eng. C 106 (2020) 110181.
[10] M. Abdullaev, A. Alhasov, D.K. Magomedova, Fabrication and properties of CuInSe 2/AgInSe 2/CdS double heterojunction cascade solar cells, Inorg. Mater. 50 (2014) 228–232.
[11] W. Sun, S.T. Dacek, S.P. Ong, G. Hautier, A. Jain, W.D. Richards, A.C. Gamst, K.A. Persson, G. Ceder, The thermodynamic scale of inorganic crystalline metastability, Sci. Adv. 2 (2016) e1600225.
[12] M. Samanta, T. Ghosh, R. Arora, U.V. Waghmare, K. Biswas, Realization of both n- and p-Type GeTe thermoelectrics: electronic structure modulation by AgBiSe2 alloying, J. Am. Chem. Soc. 141 (2019) 19505–19512.
[13] M.A. Mahdy, I. El Zawawi, The correlation of γ-irradiation, particle size and their effects on physical properties of AgInSe2 nanostructure thin films, Mater. Sci. Semicond. Process. 56 (2016) 43–51.
[14] M.A. White, K.J. Baumler, Y. Chen, A. Venkatesh, A.M. Medina-Gonzalez, A.J. Rossini, J.V. Zaikina, E.M. Chan, J. Vela, Expanding the I–II–V phase space: soft synthesis of polytypic ternary and binary zinc antimonides, Chem. Mater. 30 (2018) 6173–6182.
[15] B.A. Tappan, M.K. Horton, R.L. Brutchey, Ligand-mediated phase control in colloidal AgInSe2 nanocrystals, Chem. Mater. (2019).
[16] S. Kumar R, A. Akande, F. El-Mellouhi, H. Park, S. Sanvito, Theoretical investigation of the structural, elastic, electronic, and dielectric properties of alkali-metal-based bismuth ternary chalcogenides, Phys. Rev. Mater. 4 (2020) 075401.
[17] F. Böcher, S.P. Culver, J. Peilstöcker, K.S. Weldert, W.G. Zeier, Vacancy and anti-site disorder scattering in AgBiSe 2 thermoelectrics, Dalton Trans. 46 (2017) 3906–3914.
[18] S. Ghoshal, L.B. Kumbhare, V.K. Jain, G.K. Dey, A facile synthesis of MInSe 2 (M= Cu, Ag) via low temperature pyrolysis of single source molecular precursors,[(R 3 P) 2 MIn (SeCOAr) 4], Bull. Mater. Sci. 30 (2007) 173–178.
[19] X. Fan, J. Zhang, Y. Yang, D. Xia, G. Dong, M. Li, L. Qiu, Y. Zhang, R. Fan, Synthesis of AgBiSe2 via a facile low temperature aqueous solution route for enhanced photoelectric properties devices, J. Solid State Chem. 277 (2019) 686–692.
[20] N.D. Abazović, M.I. Čomor, M.N. Mitrić, E. Piscopiello, T. Radetić, I.A. Janković, J.M. Nedeljković, Ligand mediated synthesis of AgInSe 2 nanoparticles with tetragonal/orthorhombic crystal phases, J. Nanopart. Res. 14 (2012) 810.
[21] K. Yoshino, A. Kinoshita, Y. Shirahata, M. Oshima, K. Nomoto, T. Yoshitake, S. Ozaki, T. Ikari, Structural and electrical characterization of AgInSe2 crystals grown by hot-press method, J. Phys. Conf. Ser. (2008) IOP Publishing, pp. 042042.
[22] O. Stroyuk, A. Raevskaya, N. Gaponik, Solar light harvesting with multinary metal chalcogenide nanocrystals, Chem. Soc. Rev. 47 (2018) 5354–5422.
[23] A.P. Tiwari, T.G. Novak, X. Bu, J.C. Ho, S. Jeon, Layered ternary and quaternary transition metal chalcogenide based catalysts for water splitting, Catalysts 8 (2018) 551.
[24] Z. Liu, X. Yang, Z. Wang, H. Qi, L. Ji, X. Li, C. Ma, Z. Deng, J. Deng, Shape-controlled synthesis of water-soluble AgInSe2 nanocrystals by a convenient solvothermal approach, Mater. Lett. 161 (2015) 442–446.
[25] P. Ganguly, S. Mathew, L. Clarizia, S. Kumar R, A. Akande, S. Hinder, A. Breen, C.S. Pillai, Theoretical and experimental investigation of visible light responsive AgBiS 2 -TiO 2 heterojunctions for enhanced photocatalytic applications, Appl. Catal. B: Environ. 253 (2019) 401–418.
[26] P. Ganguly, S. Mathew, L. Clarizia, S. Kumar R, A. Akande, S.J. Hinder, A. Breen, S.C. Pillai, Ternary metal chalcogenide heterostructure (AgInS2–TiO2) nanocomposites for visible light photocatalytic applications, ACS Omega 5 (2019) 406–421.
[27] Q. Zhang, Z. Guo, X. Tan, L. Mao, Y. Yin, Y. Xiao, H. Hu, C. Tan, Q. Wu, G.-Q. Liu, Effects of AgBiSe2 on thermoelectric properties of SnTe, Chem. Eng. J. (2020) 124585.
[28] Y. Zhu, Y. Liu, M. Wood, N.Z. Koocher, Y. Liu, L. Liu, T. Hu, J.M. Rondinelli, J. Hong, G.J. Snyder, Synergistically optimizing carrier concentration and

decreasing sound velocity in n-type AgInSe2 thermoelectrics, Chem. Mater. 31 (2019) 8182–8190.
[29] L. Pan, D. Bérardan, N. Dragoe, High thermoelectric properties of n-type AgBiSe2, J. Am. Chem. Soc. 135 (2013) 4914–4917.
[30] H.-J. Wu, P.-C. Wei, H.-Y. Cheng, J.-R. Deng, Y.-Y. Chen, Ultralow thermal conductivity in n-type Ge-doped AgBiSe2 thermoelectric materials, Acta Mater. 141 (2017) 217–229.
[31] M.-A. Langevin, A.M. Ritcey, C.N. Allen, Air-stable near-infrared AgInSe2 nanocrystals, ACS Nano 8 (2014) 3476–3482.
[32] D. Che, X. Zhu, H. Wang, Y. Duan, Q. Zhang, Y. Li, Aqueous synthesis of high bright and tunable near-infrared AgInSe2–ZnSe quantum dots for bioimaging, J. Colloid Interface Sci. 463 (2016) 1–7.
[33] T. Kameyama, Y. Douke, H. Shibakawa, M. Kawaraya, H. Segawa, S. Kuwabata, T. Torimoto, Widely controllable electronic energy structure of ZnSe–AgInSe2 solid solution nanocrystals for quantum-dot-Sensitized solar cells, J. Phys. Chem. C 118 (2014) 29517–29524.
[34] L.-C. Chen, Y.-C. Ho, R.-Y. Yang, J.-H. Chen, C.-M. Huang, Electrodeposited AgInSe2 onto TiO2 films for semiconductor-sensitized solar cell application: the influence of electrodeposited time, Appl. Surf. Sci. 258 (2012) 6558–6563.
[35] P.-N. Li, A.V. Ghule, J.-Y. Chang, Direct aqueous synthesis of quantum dots for high-performance AgInSe2 quantum-dot-sensitized solar cell, J. Power Sources 354 (2017) 100–107.
[36] A.S. Kshirsagar, P.K. Khanna, Titanium dioxide (TiO 2)-decorated silver indium diselenide (AgInSe 2): novel nano-photocatalyst for oxidative dye degradation, Inorg. Chem. Front. 5 (2018) 2242–2256.
[37] G. Kresse, J. Furthmüller, Efficiency of ab-initio total energy calculations for metals and semiconductors using a plane-wave basis set, Comput. Mater. Sci. 6 (1996) 15–50.
[38] J.P. Perdew, K. Burke, M. Ernzerhof, Generalized gradient approximation made simple, Phys. Rev. Lett. 77 (1996) 3865.
[39] J. Zhang, P. Zhou, J. Liu, J. Yu, New understanding of the difference of photocatalytic activity among anatase, rutile and brookite TiO2, Phys. Chem. Chem. Phys. 16 (2014) 20382–20386.
[40] P.E. Blöchl, Projector augmented-wave method, Phys. Rev. B 50 (1994) 17953.
[41] G. Kresse, D. Joubert, From ultrasoft pseudopotentials to the projector augmented-wave method, Phys. Rev. B 59 (1999) 1758.
[42] H.J. Monkhorst, J.D. Pack, Special points for Brillouin-zone integrations, Phys. Rev. B 13 (1976) 5188.
[43] J. Heyd, G.E. Scuseria, M. Ernzerhof, Hybrid functionals based on a screened Coulomb potential, J. Chem. Phys. 118 (2003) 8207–8215.
[44] J. Heyd, G.E. Scuseria, Efficient hybrid density functional calculations in solids: assessment of the Heyd–scuseria–ernzerhof screened Coulomb hybrid functional, J. Chem. Phys. 121 (2004) 1187–1192.
[45] J. Heyd, J.E. Peralta, G.E. Scuseria, R.L. Martin, Energy band gaps and lattice parameters evaluated with the Heyd-Scuseria-Ernzerhof screened hybrid functional, J. Chem. Phys. 123 (2005) 174101.
[46] Y. Xu, M.A. Schoonen, The absolute energy positions of conduction and valence bands of selected semiconducting minerals, Am. Mineral. 85 (2000) 543–556.
[47] T.A. Hameed, A.R. Wassel, I. El Radaf, Investigating the effect of thickness on the structural, morphological, optical and electrical properties of AgBiSe2 thin films, J. Alloys. Compd. 805 (2019) 1–11.
[48] V. Aliyev, G. Guseinov, F. Mamedov, L. Chapanova, Anomalous temperature dependence of the band gap in AgGaSe2 and AgInSe2, Solid State Commun. 59 (1986) 745–746.
[49] M. Landmann, E. Rauls, W. Schmidt, The electronic structure and optical response of rutile, anatase and brookite TiO2, J. Phys. Condens. Matter 24 (2012) 195503.
[50] V. Rajaji, P.S. Malavi, S.S. Yamijala, Y. Sorb, U. Dutta, S.N. Guin, B. Joseph, S.K. Pati, S. Karmakar, K. Biswas, Pressure induced structural, electronic topological, and semiconductor to metal transition in AgBiSe2, Appl. Phys. Lett. 109 (2016) 171903.
[51] W. Chen, A. Pasquarello, Band-edge levels in semiconductors and insulators: hybrid density functional theory versus many-body perturbation theory, Phys. Rev. B 86 (2012) 035134.
[52] S. Nakatsuka, Y. Nose, Order–Disorder phenomena and their effects on bandgap in ZnSnP2, J. Phys. Chem. C 121 (2017) 1040–1046.
[53] A. Aquino Gonzalez, Physical and Optoelectronic Properties of Copper Silver Indium Diselenide Thin Films, University of Illinois at Urbana-Champaign, 2012.
[54] M.T. Ng, C.B. Boothroyd, J.J. Vittal, One-pot synthesis of new-phase AgInSe2 nanorods, J. Am. Chem. Soc. 128 (2006) 7118–7119.
[55] N. Jiang, R. Wu, J. Li, Y. Sun, J. Jian, Ethanol amine-assisted solvothermal growth of wurtzite-structured ZnS thin nanorods, J. Alloys Compd. 536 (2012) 85–90.
[56] Z. Chen, X. Qin, T. Zhou, X. Wu, S. Shao, M. Xie, Z. Cui, Ethanolamine-assisted synthesis of size-controlled indium tin oxide nanoinks for low temperature solution deposited transparent conductive films, J. Mater. Chem. C 3 (2015) 11464–11470.
[57] X. Wang, Q. Zhang, Q. Wan, G. Dai, C. Zhou, B. Zou, Controllable ZnO architectures by ethanolamine-assisted hydrothermal reaction for enhanced photocatalytic activity, J. Phys. Chem. C 115 (2011) 2769–2775.
[58] T. Bai, C. Li, F. Li, L. Zhao, Z. Wang, H. Huang, C. Chen, Y. Han, Z. Shi, S. Feng, A simple solution-phase approach to synthesize high quality ternary AgInSe 2 and band gap tunable quaternary AgIn (S 1 − x Se x) 2 nanocrystals, Nanoscale 6 (2014) 6782–6789.
[59] L. Tian, M.T. Ng, N. Venkatram, W. Ji, J.J. Vittal, Tadpole-shaped AgInSe2 nanocrystals from a single molecular precursor and its nonlinear optical properties, Cryst. Growth Des. 10 (2010) 1237–1242.
[60] H.-B. Yao, M.-R. Gao, S.-H. Yu, Small organic molecule templating synthesis of organic–inorganic hybrid materials: their nanostructures and properties, Nanoscale 2 (2010) 322–334.
[61] P. Suyana, P. Ganguly, B.N. Nair, A.P. Mohamed, K. Warrier, U. Hareesh, Co 3 O 4–C 3 N 4 p–n nano-heterojunctions for the simultaneous degradation of a mixture of pollutants under solar irradiation, Environ. Sci. Nano 4 (2017) 212–221.
[62] V. Etacheri, M.K. Seery, S.J. Hinder, S.C. Pillai, Highly visible light active TiO2 − x N x heterojunction photocatalysts, Chem. Mater. 22 (2010) 3843–3853.
[63] V. Etacheri, G. Michlits, M.K. Seery, S.J. Hinder, S.C. Pillai, A highly efficient TiO2–x C x nano-heterojunction photocatalyst for visible light induced antibacterial applications, ACS Appl. Mater. Interfaces 5 (2013) 1663–1672.
[64] S. Mathew, P. Ganguly, V. Kumaravel, J. Harrison, S.J. Hinder, J. Bartlett, S.C. Pillai, Effect of chalcogens (S, Se, and Te) on the anatase phase stability and photocatalytic antimicrobial activity of TiO2, Mater. Today Proc. (2020), https://doi.org/10.1016/j.matpr.2020.01.336.
[65] C. Xiao, Two Metal Ion Exchange Realizing Efficient Thermoelectric Properties and p–n–p Conduction Type Transition, Synthesis and Optimization of Chalcogenides Quantum Dots Thermoelectric Materials, Springer, 2016, pp. 51–64.
[66] C. Xiao, X. Qin, J. Zhang, R. An, J. Xu, K. Li, B. Cao, J. Yang, B. Ye, Y. Xie, High thermoelectric and reversible pnp conduction type switching integrated in dimetal chalcogenide, J. Am. Chem. Soc. 134 (2012) 18460–18466.
[67] Y. Jin, K. Tang, C. An, L. Huang, Hydrothermal synthesis and characterization of AgInSe2 nanorods, J. Cryst. Growth 253 (2003) 429–434.
[68] X. Kang, Y. Yang, L. Huang, Y. Tao, L. Wang, D. Pan, Large-scale synthesis of water-soluble CuInSe 2/ZnS and AgInSe 2/ZnS core/shell quantum dots, Green Chem. 17 (2015) 4482–4488.
[69] L. Shi, C. Wu, J. Ding, Effect of solvent on the synthesis of AgBiSe2 nanostructures, J. Alloys Compd. 684 (2016) 112–115.
[70] L. Devi, R. Kavitha, A review on plasmonic metal-TiO2 composite for generation, trapping, storing and dynamic vectorial transfer of photogenerated electrons across the Schottky junction in a photocatalytic system, Appl. Surf. Sci. 360 (2016) 601–622.
[71] M.M. Nakata, T.M. Mazzo, G.P. Casali, F.A. La Porta, E. Longo, A large red-shift in the photoluminescence emission of Mg1 − xSrxTiO3, Chem. Phys. Lett. 622 (2015) 9–14.
[72] P. Ganguly, M. Harb, Z. Cao, L. Cavallo, A. Breen, S. Dervin, D.D. Dionysiou, S.C. Pillai, 2D nanomaterials for photocatalytic hydrogen production, ACS Energy Lett. 4 (2019) 1687–1709.
[73] N. Padmanabhan, P. Ganguly, S. Pillai, H. John, Morphology engineered spatial charge separation in superhydrophilic TiO2/graphene hybrids for hydrogen production, Mater. Today Energy 17 (2020) 100447.
[74] P. Ganguly, S. Panneri, U. Hareesh, A. Breen, S.C. Pillai, Recent Advances in Photocatalytic Detoxification of Water, Nanoscale Materials in Water Purification, Elsevier, 2019, pp. 653–688.
[75] S. Mathew, P. Ganguly, V. Kumaravel, J. Bartlett, S.C. Pillai, Solar Light-induced Photocatalytic Degradation of Pharmaceuticals in Wastewater Treatment, Nanomaterials As Photocatalysts for Degradation of Environmental Pollutants, Elsevier, 2020, pp. 65–78.
[76] D. Sarkar, C.K. Ghosh, S. Mukherjee, K.K. Chattopadhyay, Three dimensional Ag2O/TiO2 type-II (p–n) nanoheterojunctions for superior photocatalytic activity, ACS Appl. Mater. Interfaces 5 (2013) 331–337.
[77] P. Chen, A novel synthesis of Ti3+ self-doped Ag2O/TiO2 (p–n) nanoheterojunctions for enhanced visible photocatalytic activity, Mater. Lett. 163 (2016) 130–133.